Shear-banding fluid(s) under time-dependent shear flows : Spatiotemporal dynamics (Part I)

Alice Briole, Laura Casanellas, Marc-Antoine Fardin, Charlotte Py, Olivier Cardoso, Julien Browaeys, Sandra Lerouge

Journal of Rheology

Shear-banding fluid(s) under time-dependent shear flows: spatio-temporal dynamics (Part I)

Alice Briole,[1] Laura Casanellas,[2] Marc-Antoine Fardin,[3] Charlotte Py,[1] Olivier Cardoso,[1] Julien Browaeys,[1] and Sandra Lerouge[1]

[1)]*Laboratoire Matière et Systemes Complexes, CNRS UMR 7057 Université de Paris, 10 rue Alice Domon et Léonie Duquet, 75013 Paris, France*

[2)]*Laboratoire Charles Coulomb, CNRS UMR 5221 Université de Montpellier, Place Eugène Bataillon, 34095 Montpellier Cedex 5, France.s*

[3)]*Institut Jacques Monod, CNRS UMR 7592 Université de Paris, 15 rue Hélène Brion 75013 Paris, France.*

(Dated: 28 July 2021)

We report on the response of semi-dilute shear-banding wormlike micelles to time-dependent flow protocols such as step stress and shear startup. We use global rheology coupled to direct optical visualisations in Taylor-Couette flow to provide a detailed 2D description of the spatio-temporal dynamics of the shear banding flow under imposed stress. We compare these dynamics to their extensively studied counterpart under imposed shear rate. We show that, for a given asymptotic state, the onset of banding is delayed and the transients are longer when the stress is used as control parameter. The way the banding structure is built up strongly depends on the control parameter. In the two cases, secondary flows develop on top of the shear-banding instability: after shear startup, the interface between bands is formed in the bulk of the system and migrates inwards to its stationary position in the gap of the Taylor-Couette device, before being destabilized due to elastic instability; under creep flow, the interface between bands forms at the inner wall and becomes wavy while it is still migrating outwards to its steady position, leading to permanent rearrangements of the flow structure until steady state is reached, potentially explaining longer transients. We also outline the possible mechanical signature of the onset of shear banding in terms of shape of the bulk mechanical signals, which is the subject of the second part of this work [Briole *et al.*, submitted].

I. INTRODUCTION

In complex fluids, shear banding is a flow state, in which a fluid splits into layers of differing apparent viscosities supporting different local shear rates, usually at constant stress. The coexistence of shear bands has been reported in various classes of complex systems, including polymeric fluids and soft glassy materials, suggesting that it is an emergent macroscopic phenomenon independent of many particular microscopic details of the systems. It has been observed in isotropic or organized self-assembled polymeric fluids such as surfactant wormlike micelles[17,73,95], lyotropic lamellar surfactant phases[96,97], micellar systems of block copolymers solutions[75] but also in regular polymer solutions[13,56] and in biological fluids such as DNA solutions[15] and actin solutions[58]. Shear banding is also widespread in soft glassy materials such as star polymers[93,94], emulsions[8,87], suspensions[47,50,76], colloidal gels[21,48,59] and microgels[27,29]. Depending on the system, the shear-banding flow can manifest itself transiently or as the ultimate steady state. Whatever the micro- or meso-scopic ingredients chosen to model the flow behaviour of a given class of systems, steady-state shear banding is often explained by the existence of a non-monotonic constitutive relation between shear stress and shear rate for homogeneous flow, which thus includes a region of negative slope where the homogeneous flow is unstable[104]. Note however that coupling between concentration and stress can also drive a simple shear flow unstable with respect to banding with an underlying monotonic flow curve[22,23,46]. For systems which exhibit transient banding, which heals back to homogeneous flow at steady state, the corresponding constitutive curve is expected to be monotonic. Models that predict steady shear banding often include a parameter containing the relevant ingredients specific to a given class of complex fluids, which can be tuned to restore monotonicity of the constitutive curve, accounting for transient banding. For example, the convective constraint release parameter in polymer solutions[80] or a parameter describing the competition between noise and cooperativity in soft glassy materials[9,10] can be tuned to turn banding on or off. Transient shear banding is also likely to arise in flow protocols that involve a strong time-dependence, even in fluids that do not support banding in steady shear[45,81,82].

In wormlike micelles systems, experimental evidence of an underlying non-monotonic constitutive curve dates back to the 1990s with the observation of a stress plateau independent of flow history in the measured flow curve[92]. This was the starting point of intensive experimental research sustained by strong theoretical feedback. Over the past twenty years a strong effort was made to combine global rheology with local time-resolved techniques to probe both the velocity field and the structural properties in various macro- and micro-fluidic geometries (see[28,38,62] for reviews). The understanding of shear-banded flows in wormlike micelles is

particularly advanced in TC flow, mostly because local probes are technically easier to implement in this configuration[18,30,74]. The classical scenario (or 1D picture) prescribed by the underlying non-monotonic relation was found to hold on average[95]: the flow curve is made of two increasing branches separated by a stress plateau along which the flow is heterogeneous and splits into two shear bands stacked along the velocity gradient direction. Changing the global shear rate only affects the relative proportion of each band, in a way reminiscent of equilibrium phase transitions. With the refinement of spatial and temporal accuracy, key features were also identified: first, wall slip is ubiquitous and seems deeply connected to the growth of the high-shear rate band. It manifests itself transiently and/or at steady state[33,42,69]. Second, local velocity fluctuations and associated complex flow dynamics were also found to be a quasi-systematic feature in these systems[7,43,54,63,71]. Interestingly they can remain unnoticed in the rheological signals and even in 1D velocity profiles[33,34]. Indeed, extension to 2D description revealed that the shear-banding flow in wormlike micelles is inherently unstable, the window of stability in the phase diagram being very limited[35,40]. The complex dynamics were found to mainly result from the development of secondary flows in the high-shear rate band. These secondary flows are either coherent and associated with interfacial undulations along the vorticity direction[36], or turbulent[33,89]. Unstable shear-banding flow in wormlike micelles was shown to mainly originate from viscoelastic instabilities driven by normal stresses akin to those well-known to develop in the homogeneous flow of polymer solutions with curved streamlines[83,84]. This interpretation was supported by linear stability analysis of the diffusive Johnson-Segalman model of shear banding showing that interfacial viscoelastic instabilities can also be at play[44,85].

Over the last twenty years, numerous studies have investigated the kinetics of formation of shear-banding flow in wormlike micelles in details, by trying to correlate the global response of the material with its local (structural and hydrodynamical) organisation. Even if some studies have been realized with cone-and-plate geometries[14,20], most of them have focused on the time response to step shear rate in TC flow[7,51,54,55,61,63–66,69,71,72,79,89]. In comparison, investigations of the creep response to step stress in TC flow are much more scarce[54,55]. One advantage of the TC flow lies in the non-homogeneous stress distribution due to curvature that tends to produce a plateau with a slightly positive incline, such that both the stress and the shear rate can be used as control parameters. Here, we study the time response to step stress in order to provide a detailed description of the overall shear-banding flow dynamics under creep conditions, especially over long time scales. To our knowledge such a study has not been published in the literature. Comparison with the now well-documented shear startup counterpart is also given. Note that a second part of this work[16] will be dedicated to the precise determination of the onset of banding and comparison with the case of simple yield stress fluids and theoretical predictions.

II. EXPERIMENTAL DETAILS

A. Materials

The fluid used in this study was an aqueous mixture of 0.3 M cetyltrimethylammonium bromide (CTAB) and 0.4 M sodium nitrate ($NaNO_3$) dissolved in distilled water. CTAB and $NaNO_3$ were purchased from Acros Organics and were used without purification. The sample was prepared at least one week before experiments were conducted. The mixture was initially stirred vigorously for three days and then was stored in an oven at 35°C. The temperature during the experiments was fixed to 28.0±0.1°C. This system, well-known to exhibit shear-banding, has been extensively studied in the past, in a large range of conditions, including variations of surfactant and salt concentrations and temperature[40]. The surfactant and salt concentrations chosen for the present study correspond to a weight fraction $\phi \simeq 11$ wt. %, the sample belonging to the semi-dilute concentration regime. Note that, the zero-shear viscosity of this micellar system as a function of the salt concentration at fixed surfactant concentration (0.3 M) exhibits a bell-shape variation with a single maximum around a salt concentration of 1 M[19,40]. For the salt concentration chosen here, the micellar network is not branched.

The flow dynamics of this sample has been widely explored at imposed shear rate[66] in TC flow and was shown to be generic across semi-dilute and concentrated shear banded wormlike micelles systems[28,35,40] : beyond the classical 1D shear-banding scenario, which is valid on average, the shear-banding flow was found to be unstable with respect to axial perturbations (along the vorticity direction), resulting in three-dimensional flow structures mainly located in the high-shear rate band and, ultimately, leading to elastic turbulence. For the system under study, a wide range a physico-chemical parameters was explored. The spatio-temporal dynamics is generic but subtle effects have been reported at large salt concentrations where the systems are likely to be branched[40].

B. Shear rheometry

The shear rheology of the micellar fluid was measured using a stress-controlled rheometer (Anton Paar MCR 301). The experiments were realized using a home-made TC flow geometry, with inner radius $R_i = 24$ mm, gap width $d = 1$ mm, and height $h = 40$ mm, giving a curva-

ture ratio $\Lambda \equiv d/R_i = 0.04$ and an aspect ratio $\Gamma \equiv h/d = 40$. The inner rotating cylinder was made in black Delrin®. Control experiments were also performed using a stainless steel inner cylinder. The outer cylinder was made of glass. All walls were smooth. The top of the TC cell was closed by a plug to reduce distortions of the free surface of the fluid and to avoid trapping bubbles and ejection of the sample at high shear rates. A solvent trap was also used to limit evaporation. The whole TC system was enclosed in a transparent cubic envelop that ensured temperature control *via* a circulating water bath and allowed optimisation of the optical paths for direct visualisations and particle image velocimetry experiments that were performed simultaneously with the recording of the mechanical data.

C. Optical visualisations

For many shear-banding wormlike micelles systems, the shear-induced structures contained in the high-shear rate band appear to be slightly turbid. Consequently they are likely to scatter visible light, in contrast to the native micellar structure contained in the low-shear rate band. This scattered intensity contrast between shear bands can be used to observe the banding structure and the interface between bands. In particular, direct optical visualisations in the velocity gradient-vorticity plane [(r,z) plane] can provide information about the axial and radial structure of the flow. A He-Ne laser ($\lambda = 632$ nm) and a cylindrical lens were used to generate a laser sheet propagating along the velocity gradient axis and extending along the vorticity direction to illuminate a radial plane of the TC cell. The intensity scattered by the sample at 90° was recorded by a CCD array, giving a view of the gap in the (r,z) plane. To follow the overall flow dynamics over the largest possible scale along the z direction together with a reasonable spatial resolution along the r direction, a CCD array with a fixed macro lens was used. The field of observation was centered in the middle of the cell and varied from 7 to 20 mm according to the chosen magnification.

D. Particle image velocimetry

Particle image velocimetry experiments were performed using a commercial system from Dantec Dynamics. The fluid was seeded with 100 ppm of tracer particles with a mean diameter of 5μm [Polyamide Seeding Particles (PSP), Dantec Dynamics]. A flow-velocity gradient plane [(θ,r) plane], approximately located 1 cm above the bottom of the inner cylinder, was illuminated using a Nd:YAG pulsed laser (DualPower 66-15 Laser 2x65 mJ, $\lambda = 532$ nm) equipped with optics generating a laser sheet with thickness of about 0.5 mm. Pairs of images of the (θ,r) plane were captured with a zoom-microscope lens (Zoom 6000 Navitar with a 1.5× objective and 2× adapter tube) mounted on a CCD array (FlowSense EO 4M) working at an image acquisition rate of 10 Hz. The delay between laser pulses was set to 700 μs. The steady-state velocity profiles were computed from the ready to use Dantec Dynamic studio routine using the average correlation algorithm.

E. Fluid characterisation

The micellar solution we focused on belongs to the semi-dilute concentration range, the micellar threads being organized into an entangled viscoelastic network. The storage and loss moduli, G' and G'' as a function of the angular frequency ω were measured using small angle oscillatory strain (SAOS) experiments (see Fig. 1.a). Over a large range of angular frequencies, the system was observed to behave as a single-mode Maxwell element with relaxation time $\tau = 0.24 \pm 0.05$ s and plateau modulus $G_0 = 243 \pm 5$ Pa. Here and throughout this paper, the uncertainty represents one standard deviation.

The behaviour of the sample under simple shear flow is illustrated in Fig. 1.b, which displays the evolution in semi-log scale of the shear stress σ as a function of the shear rate $\dot{\gamma}$ measured in strain-controlled mode with a sampling time of 40 s per point, large enough for the steady state to be achieved. The flow curve was measured for the sample with and without tracer particles in the TC cell configuration used for optical and velocimetry measurements, namely with the black Delrin inner cylinder. A control test with a classical stainless steel inner cylinder to check possible effect of the inner wall surface was also carried out and the result is plotted in Fig. 1.b for comparison. A resonable overlap of the flow curves in the different configurations is observed. The sample displays Newtonian behaviour with constant apparent viscosity $\eta_0 \simeq 61 \pm 1$ Pa.s for $\dot{\gamma} < 1$ s^{-1} (Fig. 1.b inset), then progressively shear-thins before reaching extreme shear thinning ($\eta \sim \dot{\gamma}^{-1}$) above $\dot{\gamma} \equiv \dot{\gamma}_1 \simeq 4.5 \pm 0.5$ s^{-1} where the shear stress reaches a stress plateau at $\sigma \equiv \sigma_p \simeq 155 \pm 3$ Pa, indicative of gradient shear banding[98,99]. Finally, the stress plateau ends around $\dot{\gamma} \equiv \dot{\gamma}_2 \simeq 73 \pm 5$ s^{-1} and the flow curve exhibits an increasing high-shear rate branch, which is characteristic of the rheology of the shear-induced structures. Due to the intrinsic curvature of the flow geometry, the stress plateau is not flat but exhibits a positive slope in contrast to what is expected in flows with homogeneous stress distribution such as the (small-angle) cone-and-plate flow. One can then take advantage of this flow geometry to explore the flow dynamics in the shear-banding regime at both imposed shear rate and shear stress. Note that secondary flows in the shear-banding regime were also shown to contribute to the slope of the stress plateau[66]. Along the stress plateau, the flow becomes non-homogeneous and the fluid supports two states of different apparent viscosities and local shear

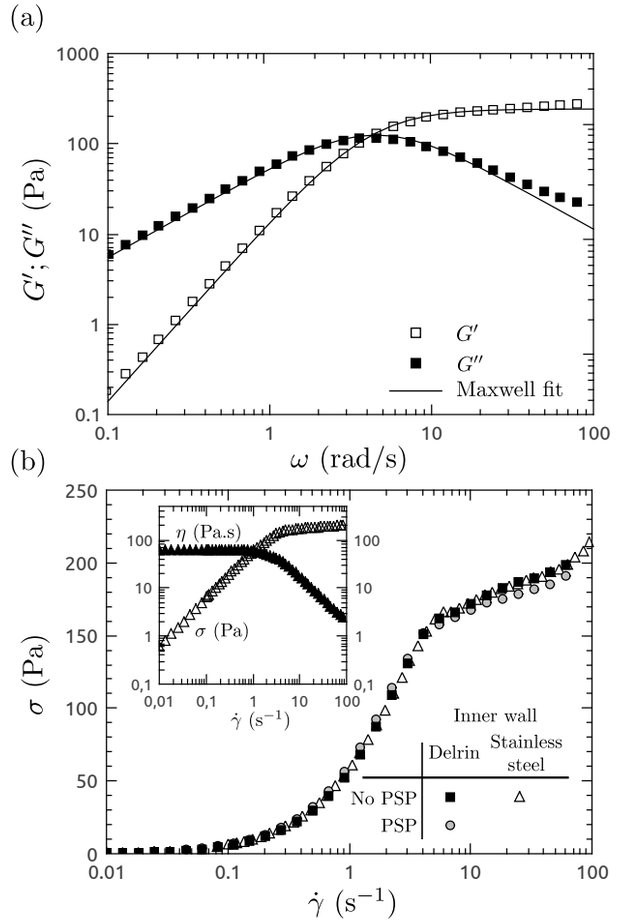

FIG. 1. (a) Storage and loss moduli, G' and G'' as a function of the angular frequency ω for an imposed strain $\gamma = 5\%$. The continuous lines represent the best fit obtained from a single-mode Maxwell model. (b) Steady-state flow curve measured using shear sweep mode with sampling time of 40 s per data point, in TC cell with inner cylinder in black Delrin for sample without PSP (■) and with PSP (○). Test with stainless steel inner cylinder for sample free of PSP (△). Inset : Shear stress σ (△) and apparent viscosity η (▲) as a function of the shear rate $\dot{\gamma}$ in log-log scale.

rates as illustrated in Fig. 2, where time-averaged velocity profiles are reported for various applied shear stresses along the stress plateau. Basic fitting procedure of the local velocity with linear function provides estimates of the local shear rates $\dot{\gamma} \equiv \dot{\gamma}_l \simeq 4.0 \pm 0.2$ s^{-1} and $\dot{\gamma} \equiv \dot{\gamma}_h \simeq 66 \pm 5$ s^{-1} in the low- and high-shear rate bands respectively. These values are compatible with the critical shear rates $\dot{\gamma}_1$ and $\dot{\gamma}_2$ characterising the limits of the stress plateau. Note however that $\dot{\gamma}_2$ cannot always be determined unambiguously from the flow curve due to possible transition towards elastic turbulence in the high-shear rate band[40]. The velocity profiles were recorded simultaneously with the shear rate time series. From the asymptotic value of the shear rate, the velocity expected at the inner moving wall, in the absence of slip,

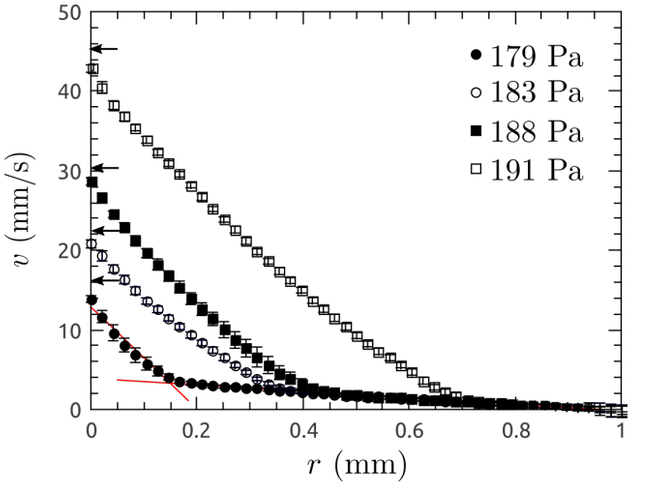

FIG. 2. 1D time-averaged velocity profiles measured using PIV technique for various imposed shear stresses along the stress plateau. Each profile results from averaging over 50 pairs of images. The error bars correspond to the standard deviation. The arrows along the y-axis denote the velocity expected at the inner wall and computed from the asymptotic value of the measured shear rate. Red lines correspond to basic fitting with a linear function to provide estimates of the local shear rates $\dot{\gamma}_l$ and $\dot{\gamma}_h$ in each band.

can be computed and compared to the effective velocity measured locally. In Fig. 2, the velocities expected at the moving wall are denoted by arrows along the y-axis. For all imposed shear stresses, noticeable slip is observed at the moving wall, a feature that is ubiquitous in shear-banding wormlike micelles[33,69]. The slip velocity is, on average, equal to 10 to 20% of the wall velocity.

III. RESULTS AND DISCUSSION

A. Bulk rheological time responses

As mentioned in the introduction, studies focusing on the time response of shear-banding wormlike micelles under controlled shear stress remain very limited[54,55] compared to their controlled shear rate counterpart[7,51,54,55,63–66,69,71,72,79,89].

Figure 3.a displays the time response of the global shear rate to various stresses applied from $t = 0$ to a sample initially at rest. The applied stresses are all associated with a shear-banded state at steady state. For all applied shear stresses, the time evolution of the shear rate is essentially the same. It is simply more contracted in time as the control parameter goes away from the lower boundary of the stress plateau. The early stages of the shear rate response to various representative step stresses are illustrated in figure 3.a.left. The initial response (typically $t \lesssim 0.5$ s) is dominated by damped oscillations (Fig. 3a.left.inset), exactly as reported in Ref.[55]

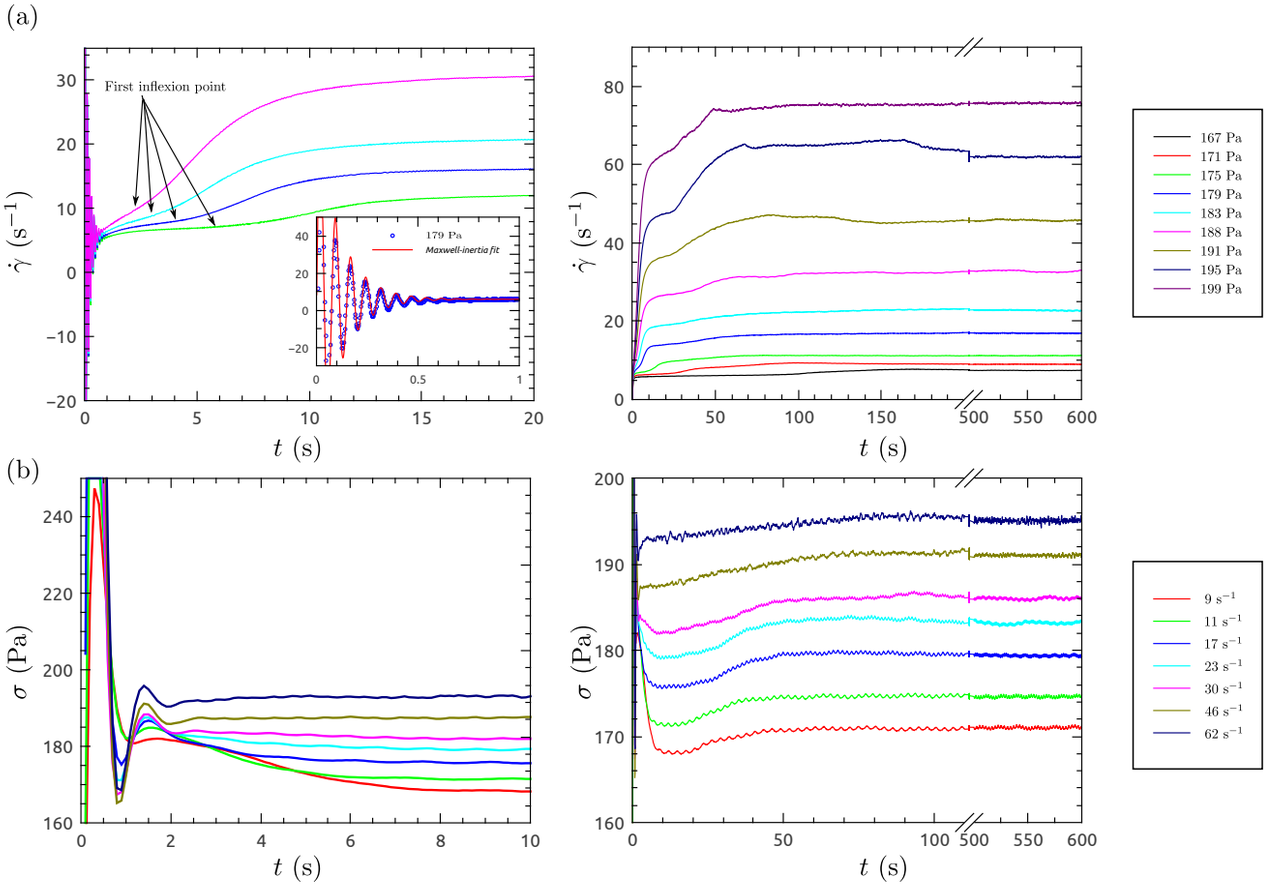

FIG. 3. (a) Temporal evolution over short (left) and long (right) time scales of the global shear rate following step stress applied at $t = 0$ to a sample initially at rest. All the applied stresses span the stress plateau. Inset: Magnification of early stages of the response for $\sigma = 179$ Pa. The sampling time is 3 ms. The red line corresponds to the best fit using a Maxwell model coupled to instrumental inertia[4] [see Eqn (1)].(b) Temporal evolution over short (left) and long (right) time scales of the shear stress following shear startup applied at $t = 0$ to a sample initially at rest.

on a similar wormlike micelles system. This behaviour observed under stress-input conditions is very general across complex fluids and is due to the coupling between the sample elasticity and the instrument rotational inertia, leading to some kind of resonance phenomenon called inertio-elastic ringing[4,5,31,32,103]. Following Ref.[4], coupling between the equation of motion of the inner rotating cylinder and the scalar Maxwell constitutive law was used to fit the data (see Fig. 3a.left.inset):

$$\dot{\gamma}(t) = \frac{\sigma_0}{\eta}\left\{1 - \exp\left(\frac{-Gt}{2\eta}\right)\left[\cos\omega t + \frac{1}{\omega}\left(\frac{G}{2\eta} - \frac{\eta}{a}\right)\sin\omega t\right]\right\} \quad (1)$$

where σ_0 is the applied stress, η and G are the parameters of the Maxwell model, $\omega = \sqrt{G^2/4\eta^2 - G/a}$ is the ringing frequency and $a \equiv I\frac{F_\sigma}{F_\gamma}$ involves the moment of inertia I of the mobile part of the instrument and the conversion factors used to compute stress (F_σ) and strain (F_γ) respectively from the torque and displacement. For an imposed stress $\sigma = 179$ Pa, the parameters resulting from the best fit were found to be $G = 8.5$ Pa, $\eta = 1.7$ Pa.s and $\omega = 84$ rad/s. From G and η, a characteristic time $\tau = 0.2$ s can be built, which is 20% smaller than the relaxation time of the system. The values of G, η and τ are difficult to interpret, especially in a situation where the nonlinear regime at steady state is dominated by coexistence of different states of the system. For the range of applied shear stresses explored here, the instantaneous deformation during ringing can reach values as high as 4. By making a parallel with observations made in large amplitude oscillatory strain or stress experiments, the microstructure of the sample is likely to be strongly oriented in a homogeneous way across the gap[52], the duration of the largest oscillations being too short for a separation into bands to be established. As the ringing frequency is much larger than $1/\lambda$, the microstructure may not be able to relax towards a state close to its quiescent state. Hence, η and G obtained from the fitting procedure might reflect the order of magnitude of the viscoelastic properties of the microstructure in a flow-aligned and disentangled state

similar to the one observed in shear- startup[63,65,70] and preceding the onset of banding. In particular, the value of η is fully compatible with the apparent viscosity of the system measured at the beginning of the high-shear rate branch. The values of G and τ might also reasonably describe the viscoelastic properties of the shear-induced state, which is less entangled than the quiescent state and was shown to relax within time scales close to τ_R[52,54].

The inertio-elastic ringing regime is followed by a stage where the measured shear rate is constant or slightly increasing, depending on the applied stress. Following Hu *et al.*, this regime is called 'the induction period', the flow remaining homogeneous during this stage[55]. The duration of the induction period drastically decreases with increasing shear stress (it is about 100 s at 167 Pa but becomes almost imperceptible in linear scale above 183 Pa), in agreement with early findings by Grand *et al.*[49] and more recent results by Pipe *et al.*[90]. The end of the induction period is marked by an inflexion point (the first inflexion point mentioned in Fig. 3.a.left), the curvature of the shear rate curve changing from negative to positive. Beyond this first inflexion point, the subsequent stage is associated with an increase of the shear rate towards its steady-state value, which is rather smooth at 167 Pa but presents at least two distinct variation rates at higher stresses: a steep growth of $\dot{\gamma}(t)$, which extends typically over 10 s followed by a slower one of duration ranging between 20 and 60 s with decreasing stress. For the largest applied shear stresses ($\sigma \geq 191$ Pa), variations around the steady-state value are sometimes observed at long times ($t \geq 150$ s, see Fig. 3.a right). We will see in the following that these variations are most likely related to rearrangements of 3D flow structures.

For step shear rates, the stress response has been comprehensively studied for decades[11,12,49,52,54,55,66]. Here we limit ourselves to recalling its main features. Figure 3.b illustrates the typical shear stress response to shear startup of a sample undergoing a shear-banding transition. At very short times ($t \simeq \tau$) the shear stress was shown to exhibit an overshoot, the amplitude of which notably increases with increasing applied shear rate. The stress relaxation from the stress maximum towards steady-state occurs over different times scales. The first relaxation process is fast (of the order of a few relaxation times) and corresponds to a stress drop from the maximum while the second one can be much longer, especially for applied shear rates close to the first critical shear rate, *i.e.* in the metastable region of the constitutive curve (Fig. 3.b.right). Depending on the applied shear rate, this second relaxation process is characterized either by a stretched exponential evolution with characteristic time increasing as the applied shear rate approaches the first critical shear rate $\dot{\gamma}_1$ or by damped oscillations at larger shear rates (Fig. 3.b.left). The subsequent evolution is a slow increase (or small undershoot) of the shear stress to its steady-state value with a very weak relative stress increment (between 1 to 2%), which may remain unnoticed but which is a robust feature that can be observed on most shear stress time series recorded for shear-banding wormlike micelles both in TC and CP flows[11,49,52,54,66].

B. Formation of the banding structure.

We used direct visualisations of the gap of the TC cell in the (r,z) plane to follow the formation and the evolution of the shear-banding structure during creep and shear start-up tests performed on the sample initially at rest. The temporal sequence in creep flow is given in Fig. 4.a for an applied shear stress $\sigma = 183$ Pa. The first 40 s of the sequence together with the final snapshot at $t = 600$ s are shown. At $t = 0$, the sample is at rest and the gap appears dark. As a constant shear stress is applied, the sample scatters visible light very slightly in a homogeneous way across the gap ($t = 1.6$ s). The appearance of turbidity is widespread in shear-banding wormlike micelles systems, especially for semi-dilute ones[37,63]. This behaviour is connected to the butterfly patterns observed in small angle light scattering experiments[24,54,57,100], which are most likely related to flow/concentration coupling[53]. Then quickly ($t \simeq 2$ s) the level of scattered intensity starts growing from the inner wall. It is difficult to distinguish a banded structure at this stage because the interface is very broad and diffuse. At $t = 4.2$ s, a banding structure is clearly visible: a small bright band at the inner wall coexists with a dark band adjacent to the outer wall. The scattered intensity in the bright band is reinforced while the interface between bands becomes better defined. As time evolves from $t = 6.4$ s, the level of scattered intensity in the shear-induced band seems to saturate while the interface between bands becomes sharper and moves towards the outer wall. Around $t \simeq 16$ s, the first signs of interface destabilisation along the vorticity direction appear. Between $t = 17$ s and $t = 24$ s, the size of the shear-induced band slightly reduces and modes of shortest wavelength seem to take place. However, from $t = 24$ s, the size of the shear-induced band starts growing again while secondary flows fully develop leading to interfacial undulations. From $t = 30$ s, the amplitude of the dominant mode is very close to the amplitude of the asymptotic mode (see snapshot at $t = 600$ s) whereas the wavelength evolves with time as the size of the shear-induced band keeps increasing. The full spatio-temporal dynamics over the whole sequence will be given in the next section.

After a step shear rate, the formation of a banding structure follows a very different scenario. Detailed 2D description of the kinetics of formation of the banding structure at imposed shear rate can be found elsewhere for different semi-dilute and concentrated micellar systems[33,41,66]. We recall here the main steps of the scenario, which was demonstrated to be generic over a very large region of the phase diagram[40,41]. Fig. 4.b depicts a se-

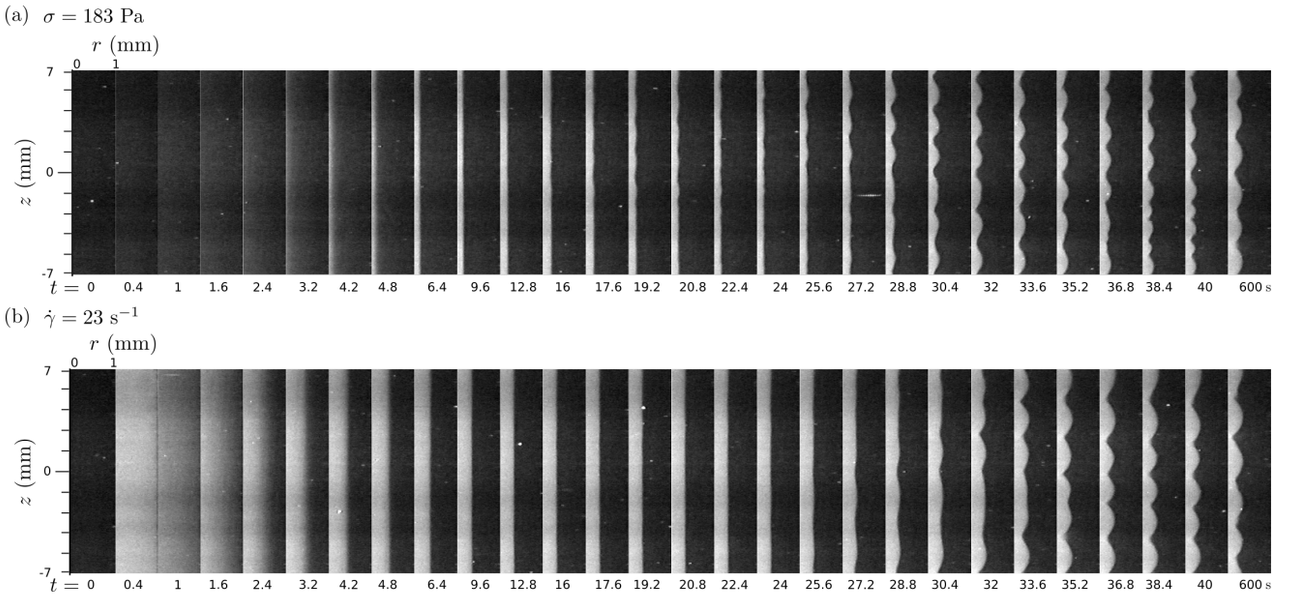

FIG. 4. Temporal series of scattered intensity map recorded in the (r,z) plane. The left and right sides of each picture are associated with the inner rotating and the outer fixed cylinders respectively. The field of observation is limited to 14 mm and centred at mid-height of the inner cylinder (position at $z = 0$). The sample is initially at rest ($t = 0$). The total duration of the experiment is 600 s. (a) Creep experiment with applied stress $\sigma = 183$ Pa. (b) Shear start-up experiment with applied shear rate $\dot{\gamma} = 23$ s^{-1}, corresponding to the asymptotic value of the shear rate measured in (a).

quence of snapshots recorded for an applied shear rate $\dot{\gamma} = 23$ s^{-1}, which corresponds to the asymptotic value of the shear rate measured during creep flow at $\sigma = 183$ Pa (see Fig. 3.a). Just after the startup of flow, the sample, initially transparent, becomes turbid across the whole gap and the level of scattered intensity reaches a maximum before diminishing in a uniform way. From $t \simeq 1$ s, a diffuse interface builds up near the fixed outer cylinder, migrates toward the inner rotating cylinder while progressively sharpening. As the interface adopts a fixed sharp profile, it keeps moving toward its stationary position ($t \simeq 17$ s). Finally, around $t \simeq 25$ s, 3D shear-banding flow develops and the interface starts undulating along the vorticity direction.

In the next section, we will see how these dynamics are related to the time evolution of the global mechanical variables.

C. Spatio-temporal dynamics in the banding regime.

In order to correlate the global response of the system with its behaviour at local scale, spatio-temporal diagrams summarizing the interface dynamics (or equivalently the flow dynamics) were built as explained below and are shown in Fig. 5. At a given value of the control parameter (σ or $\dot{\gamma}$), the level of scattered intensity was extracted by thresholding of each frame in the stack recorded at 5 fps (like the ones exemplified in Fig. 4). The threshold was adjusted to the value of the intensity in the shear-induced band. This is equivalent, as an interface emerges, whether diffuse or sharp, to detect the position of the interface profile $r_i(z)$ with $r_i \in [0, d = 1$ mm$]$, the origin being taken at the inner moving wall. The spatio-temporal diagram $r_i(z,t)$ was constructed by encoding in grey levels the interface position r_i as a function of time and space coordinates. Hence, black or dark grey regions correspond to positions of the interface closer to the inner cylinder than white or light grey regions (see Fig. 5.c). Spatio-temporal dynamics of the shear-banded state are given in Fig. 5.a0 to a5 for creep flow and in Fig. 5.b1 to b5 for shear startup. The temporal evolution of the corresponding measured global variable (green line) and of the interface mean position $\langle r_i(t)\rangle_z$ (red line) are superimposed to the diagrams to make the correlation easier.

Let us first focus on the response of the system to creep flow (Fig. 5 left column). After creep ringing ($t \lesssim 0.5$ s, not visible in the diagrams), the measured shear rate reaches a first level (the induction period), during which $r_i(z,t)$ is equal to zero (black regions at the beginning of each diagram - see also $\langle r_i(t)\rangle_z$ in red) : the banding structure has not yet emerged and the flow remains homogeneous. The banding structure is observed to emerge at the very beginning of the subsequent stage, which starts at the first inflexion point in $\dot{\gamma}(t)$ mentioned earlier, and corresponds to a relative steep growth of $\dot{\gamma}(t)$. The shear-induced band nucleates from the inner wall and the interface between bands moves towards its stationary position in direction of the outer cylinder. The growth of the shear-induced band is faster as the

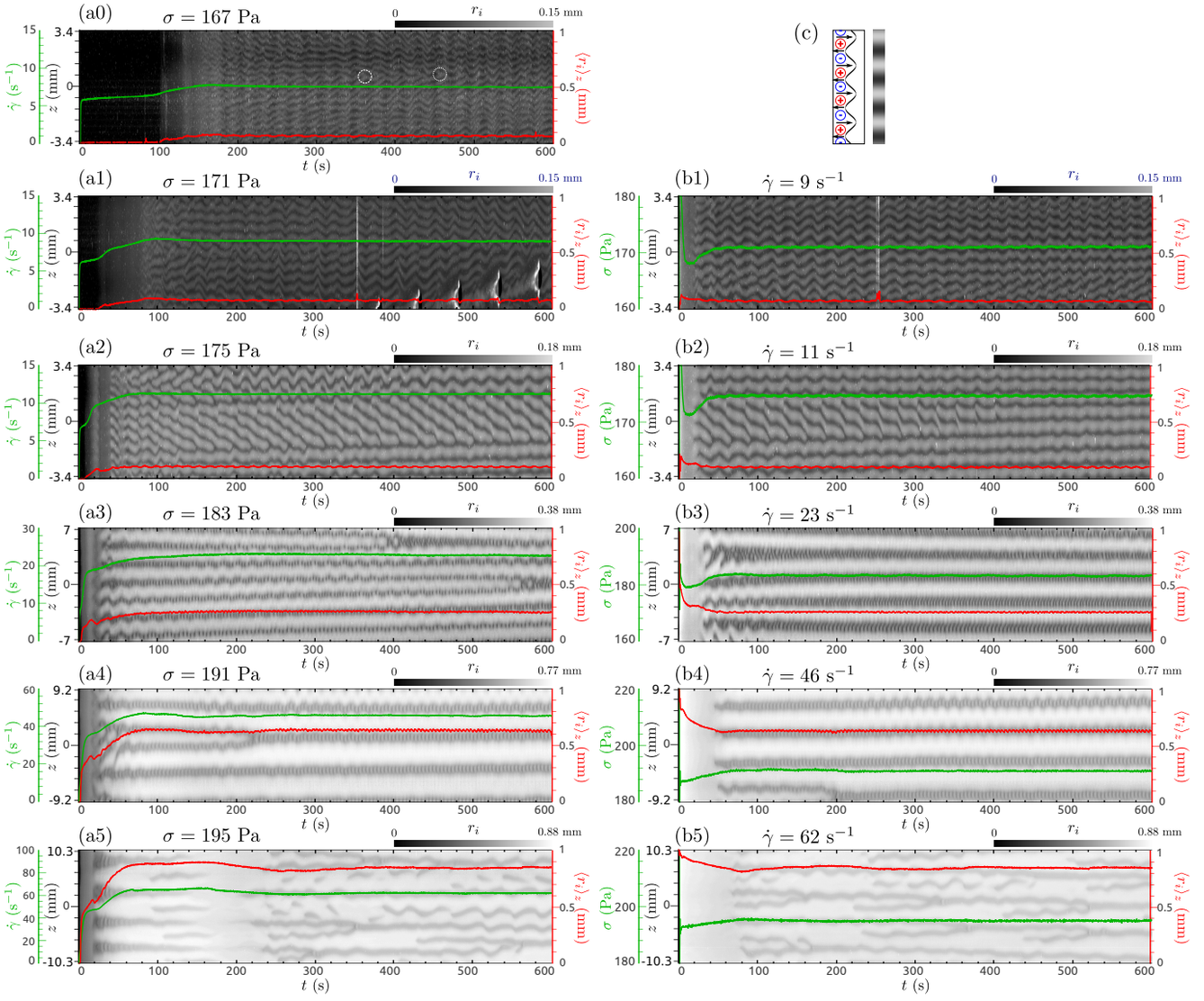

FIG. 5. Spatio-temporal diagrams summarizing the interface dynamics (or equivalently the flow dynamics) following creep flow (left column) and step shear rate (right column). For step shear rate experiments, the imposed shear rate was fixed to the asymptotic value measured during creep experiments, that is, the asymptotic states between a diagram on the left (a1 to a5) and on the right (b1 to b5) of the figure are the same. The interface position r_i is encoded in grey level as a function of the time and the spatial coordinate along the cylinder axis (z-coordinate). The origin is taken at the inner moving wall. The value of the control parameter (σ or $\dot{\gamma}$) is specified on top of each diagram. Green lines represent the time series of the corresponding response ($\dot{\gamma}$ or σ) with a temporal resolution of 0.2 s/pt while red lines are associated with the temporal evolution of the interface position $\langle r_i(t) \rangle_z$ averaged over z. The white dot circles in (a0) mark processes of annihilation of pair of vortices separated by an inward radial flow. Note that the white and black patches apparent in diagram a1 are due to a rising bubble. (c) Sketch illustrating the wavy interface and the concomitant Taylor-like vortices in the high-shear rate band. Inward and outward radial flows are displayed. The resulting position of the interface in grey levels used for the construction of the spatio-temporal diagrams is also shown.

applied shear stress increases. From the whole set of data a0 to a5, we can already anticipate that the first inflexion point in $\dot{\gamma}(t)$ is closely connected to the onset of banding (compare red and green curves especially at the lowest applied stresses). This particular stage will be studied in detail in the second part of this work[16]. Note that the motion of the interface between bands is not monotonic. Whatever the applied stress, we systematically observe a small bump in the mean interfacial position $\langle r_i(t) \rangle_z$. A small reduction of the grey level at that particular time is also visible. The interface slightly goes back before moving outward again. Finally, destabilisation of the interface along the vertical direction occurs due to the development of secondary flows in the high-shear rate band[36]. For the smallest stresses explored here, the destabilisation process takes place while

the global shear rate and the interface position are approaching their steady-state values. For the largest applied stresses, the interface becomes wavy while it keeps moving outward and is far from having levelled off at its final position. It is however difficult to relate both the local backward motion of the interface and the onset of the elastic instability to specific variations in the global shear rate, especially for the smallest imposed stresses (σ = 167 and 171 Pa) where the thickness of the shear-induced band does not exceed 150 μm. For the largest imposed stresses, the local backwards motion happens around 20 s and seems concomitant with the onset of elastic instability. The time evolution of the global shear rate described above was already reported for a different shear-banding wormlike micelles system [cetylpyridinium chloride (CPCl)/sodium salycilate (NaSal)] by Hu *et al.*, who also examined the correlation with the velocity field[54,55]. The velocity profiles were found to be linear during the induction period in the global shear rate response, beyond which a high-shear rate band was observed to nucleate from the inner cylinder. Note that a similar trend was also reported in cone-and-plate flow[14]. These features are in full agreement with our observations.

For step shear rates, the correlation between the stress response and the behaviour of the system at local scale has been comprehensively studied for decades[52,54,55,63,89]. At very short times ($t \simeq \tau$) the stress overshoot is connected to the appearance of turbidity in the whole gap. Flow birefringence and neutron scattering experiments have shown that the micellar threads are concomitantly oriented and stretched with respect to the flow direction[52,65,79]. The fast relaxation of the stress overshoot was found to correspond to homogeneous reduction of the turbidity. The characteristic sigmoidal relaxation and possibly the damped oscillations that followed were related to the formation, migration and sharpening of the interface profile between bands towards its stationary position in the gap of the TC cell. Finally, the last stage in the shear stress evolution was observed to be an undershoot of small amplitude (see Ref.[49,66] for example), which was associated with the migration of the interface driven by stress diffusion[41,67] followed by the development of 3D shear-banding flow due to elastic instability in the high-shear rate (turbid) band[40].

Following the spatio-temporal dynamics of the interface between bands provides direct information about the axial structure of the flow and its dynamics. Indeed, it has been shown that the observed patterns are completely correlated to the flow patterns obtained from flow visualisations[36,88] or 2D velocimetry measurements[88,89]. The interface between band starts undulating due to secondary flows that develop in the high-shear rate band[35,36]. Thus, the wavy interface is a signature of the presence of pairs of counter-rotating vortices mainly located in the high-shear rate band. To make the reading of the diagrams easier, a sketch of the axial structure of the flow and its relation with the grey scale of the diagrams is depicted in Fig. 5.c. The light and dark grey zones correspond to outflow and inflow regions respectively. The dynamics of secondary flows have been described at length in the literature in the case of step shear rate for a curvature ratio $\Lambda = 0.08$[40,66]. The main patterns identified for this control parameter are similar for $\Lambda = 0.04$ and are shown here in the right column in Fig. 5 for direct comparison with the case of creep flow (left column).

The patterns following step stress and step shear rate are essentially the same and just differ by the transient behaviour. Note that ten minutes is the minimum duration for the asymptotic state to be achieved in stress-controlled mode. In the two cases, the flow pattern are found to depend on the applied stress or shear rate. As the size of the high-shear rate band increases with the control parameter, the size of the vortices which mainly occupy this band is affected. It was indeed found that the wavelength of the wavy interface scales as the size of the high-shear rate band[40].

For small widths of the shear-induced band, the vortex flow is oscillating along the vorticity direction in a characteristic zig-zag pattern. Note that for shear-banded concentrated systems close to the zero-shear isotropic–nematic phase transition, which were also found to be unstable[35], such patterns could be related to periodical spatial fluctuations of both the order parameter and the angular deviation from the vorticity axis[1,2]. Waves propagating towards the top or the bottom of the cell can also superimpose to the zig-zag pattern (Fig. 5.b1, a2, b2). The thickness (along z) of the light and dark grey regions is very similar, suggesting that the aspect ratio of the vortices is close to one. Note that for the smallest applied shear stress, a few events associated with the annihilation of pairs of counter-rotating vortices separated by an outflow can be observed (see white dot circles in Fig. 5.a0). Such events have already been observed at imposed shear rate but further along the stress plateau[40].

For intermediate widths of the high-shear rate band, the zig-zag pattern is observed transiently, as well as a few processes of annihilation of pair of vortices separated by an outward radial flow. The asymptotic state corresponds to a stationary vortex flow, with the boundaries of the vortices oscillating slightly with a period that is about one order of magnitude larger than the relaxation time (see periodic tiny stripes located in the inflow regions of the diagrams in Fig. 5.a3, b3, a4, b4). The relative thickness of the light and dark regions is modified suggesting that the aspect ratio of the vortices changes with increasing control parameter. The vortices appear more extended along the vorticity direction than in the radial direction, which is a typical feature of the flow structures triggered by the elasticity[6].

Finally, for the largest widths of the high-shear rate

band, continuous processes of generation and annihilation of pairs of vortices take place in a way reminiscent of the flame pattern observed as polymer solutions undergo purely elastic or inertio-elastic instability in TC flow[101,102]. Again, comparison between stress- and strain-controlled modes shows that the transient are very different: the elastic instability is triggered earlier under creep flow (Fig. 5.a5); the pattern first looks like a regular vortex flow and then presents a period doubling around $t \simeq 100$ s before vanishing around $t \simeq 180$ s. Generation and annihilation of pair of vortices eventually start after $t \simeq 210$ s, while this particular spatio-dynamical behavior is established around $t = 90$ s when the shear rate is applied (Fig. 5.b5).

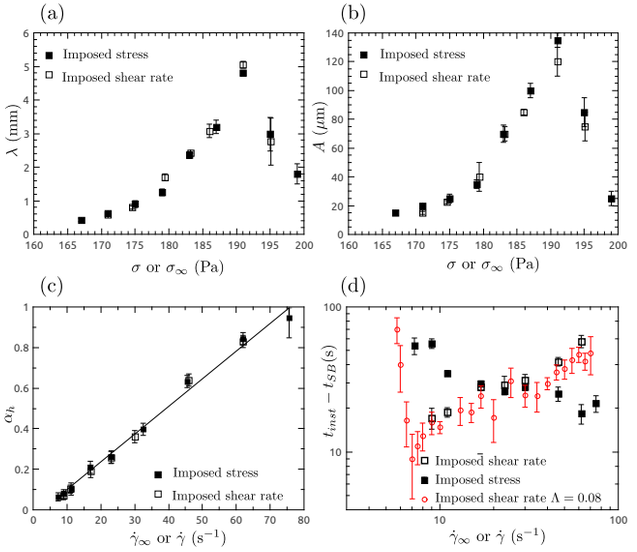

FIG. 6. (a) Asymptotic wavelength λ as a function of the imposed stress σ (■) or the asymptotic stress σ_∞ (□) when the shear rate is used as control parameter. (b) Asymptotic amplitude A of the pattern as a function of the imposed stress σ (■) or the asymptotic stress σ_∞ (□) when the shear rate is used as control parameter. (c) Classical 'lever rule' representation: The proportion of the high-shear rate band α_h is plotted as a function of the applied shear rate (□) or the asymptotic shear rate $\dot{\gamma}_\infty$ (■) when the controlled-stress mode is used. The black line corresponds to a linear fit according to a simple lever rule. (d) Time characterising the beginning of the interface instability after step stress (■) or step shear rate (□). The time reference t_{SB} is taken as the banding structure nucleates. Data at imposed shear rate from Ref.[66] are plotted for comparison (red ○).

In Figs. 6.a and b, we have summarized the asymptotic wavelength λ and amplitude A of the patterns. They are plotted as a function of the imposed shear stress σ or the asymptotic shear stress σ_∞ when operating at imposed shear rate. As expected, they follow the same non-monotonic trend whatever the control parameter. λ increases with σ or $\dot{\gamma}$ consistently with the fact that the Taylor-like vortices mainly develop in the high-shear rate band[36], their size increasing as the interface moves outward. A drastic reduction is however observed as the vortices start interacting with the outer wall, typically when the flame pattern dominates the dynamics. The wavelength reaches a maximum ($\lambda_{max} \simeq 5$ mm) as the two bands are approximately in equal proportions in the gap. As the influence of the walls is reduced in this situation, the amplitude of the pattern is also maximum ($A_{max} \simeq 120$ μm). The asymptotic state was also used to compute the proportion of the shear-induced structures α_h in the gap as a function of the control parameter by integration of the interface profile over z (Fig. 6.c). In a classical representation as a function of the applied shear rate $\dot{\gamma}$ (or asymptotic shear rate $\dot{\gamma}_\infty$ when the stress is imposed), α_h is found to follow a simple lever rule $\alpha_h = (\dot{\gamma} - \dot{\gamma}_l)/(\dot{\gamma}_h - \dot{\gamma}_l)$. A linear fit gives the following parameters $\dot{\gamma}_l = 3.2\ \mathrm{s}^{-1}$ and $\dot{\gamma}_h = 75\ \mathrm{s}^{-1}$. The estimate of the first critical shear rate is clearly underestimated while the value of the second critical shear rate is compatible with $\dot{\gamma}_2$ extracted from the flow curve. As shown previously, the linear fit is not a sufficient description. Wall slip and flow instabilities might be responsible for the slight deviation from the simple lever rule[33,37,66].

Even if the flow dynamics at long time do not depend on the nature of the control parameter, the transient dynamics do. Generally, the duration of the transients is longer at imposed stress than at imposed shear rate. In particular, the emergence of the banding structure happens earlier as $\dot{\gamma}$ is used as control parameter and rearrangements of pairs of vortices can spread over much longer time scale as stress is applied (see Fig. 5a3 and a5 for example). Note that a similar situation has been reported in yield stress fluids: in carbopol microgels, fluidization under a given shear stress was found roughly ten times slower than fluidization under the corresponding shear rate, the duration of the slip regime being strongly dependent on the control parameter[26].

As mentioned in the previous section and as illustrated in Fig. 5 by direct comparison of the evolution of $\langle r_i(t)\rangle_z$ (red lines) between the left and right columns, the interface does not form at the same location in the gap of the TC cell. In strain-controlled mode, the interface forms in the bulk (even close to the outer cylinder for sufficiently high applied shear rates) and moves towards the inner cylinder to reach its steady position while in controlled-stress mode, the interface nucleates close to the inner moving wall and migrates outward to its final position. Furthermore, the time, at which the elastic instability starts developing does not evolve in the same way. Fig. 6.d displays the time $t_i = t_{inst} - t_{SB}$ elapsed between the early stage of formation of the banding structure and the trigger of the elastic instability for each control parameter. The data are plotted as a function of the applied or asymptotic shear rates, depending on the control parameter ($\dot{\gamma}$ or σ). Previous results[66] obtained in strain-controlled mode over an extended range of $\dot{\gamma}$ and for $\Lambda = 0.08$ are also shown for comparison. For imposed shear rates at the beginning of the stress plateau, t_i abruptly decreases before increasing as $\dot{\gamma}$ ex-

ceeds about 8 s^{-1}, which is very close to the local maximum (spinodal point) of the underlying non-monotonic constitutive curve[11,66]. In contrast t_i monotonically decreases with increasing applied shear stress. Hence, for asymptotic flow states such as $\dot{\gamma} \lesssim 17$ s^{-1} ($\dot{\gamma}\tau \lesssim 4$), the instability of the shear-banding flow appears earlier at imposed shear rate than under imposed stress. Conversely, for asymptotic flow states such as $\dot{\gamma} \gtrsim 40$ s^{-1} ($\dot{\gamma}\tau \gtrsim 9$), the instability of the shear-banding flow develops earlier when the stress is applied. By analogy with the homogeneous flow of polymer solutions[60,86], the onset of elastic instability in the high-shear rate band was suggested to depend on the local shear rate $\dot{\gamma}_h(t)$ in this band and the local curvature ratio $\alpha_h\Lambda$[39]. During the transient both α_h and $\dot{\gamma}_h$ evolve with time, the influence of the latter being prevailing (the instability threshold is expected to scale as $\dot{\gamma}_h(t)$ and $\sqrt{\alpha_h}$). The different trends in strain- or stress-controlled modes suggest that the way $\dot{\gamma}_h$ is established for a given control parameter *i.e.*, for a given asymptotic flow state, depends on its location on the stress plateau.

Hu *et al.* investigated the flow field dynamics of a similar system (CPCl/NaSal) for a few values of the control parameter ($\dot{\gamma}$ and σ)[54,55]. They observed that the building of the high-shear rate band is radically different at imposed stress or imposed shear rate, in agreement with the optical visualisations of figure 4. In stress-controlled mode, the velocity profile were found to be linear across the gap during the induction period. They became curved as the mean shear rate started increasing just beyond the induction period and were found to quickly adopt a banded profile. As the high-shear rate band expanded outward to reach its final position, the local slope in the high-shear rate band was observed to remain fixed, $\dot{\gamma}_h$ having reached its asymptotic value. In strain-controlled mode, the velocity profiles were observed to become progressively curved and the migration of the interface was seen as an expansion of the low-shear rate band inward. During the whole process, the local slope in the high-shear rate band was observed to become steeper and steeper. Such differences might be an argument to explain that the instability threshold can be reached at different times in the two control modes. However, the detailed work by Hu *et al.*[54,55] did not cover the whole stress plateau. To the best of our knowledge, a systematic and comparative study of the dynamics of the velocity field along the stress plateau in both stress- and strain-controlled modes remains to be performed. It could also bring interesting information about the value of the elastic instability threshold.

IV. CONCLUSIONS

In the present study we provided the first detailed 2D description of the whole spatio-temporal flow dynamics under imposed stress of shear-banding wormlike micelles, which was absent in the literature so far. At short time, the shear rate response is dominated by inertio-elastic ringing, the analysis of which could bring quantitative information about the viscoelastic properties of the shear-induced structures. The onset of banding under creep flow seems related to a particular mechanical signature in terms of shape of the bulk shear rate signal. This point will be addressed in detail in the second part of this work[16]. Comparison between creep flow 2D dynamics and its extensively studied counterpart at imposed shear rate shows that for a given asymptotic state, the onset of banding is delayed and the transients are longer when the stress is used as control parameter. Furthermore the formation of the banding structure is completely different in the two cases. At imposed stress, the high shear rate band emerges from the inner wall and the interface moves progressively outwards to its steady position. This difference is explained by the existence of a stress overshoot at imposed shear rate due to the elasticity of the micellar network. During the overshoot, the shear stress in the whole gap is much larger than the stress plateau. The sample experiences shear stresses associated with the high-shear rate branch of the flow curve. As the stress plateau value fixes the steady-state position of the interface, the inward motion of the interface to its steady position following shear start-up is then prescribed by the overshoot. In stress-controlled mode, the stress at the wall is fixed and decreases as a function of the radial coordinate due to curvature inherent to the TC flow. In this mode, the global shear rate progressively increases to accommodate the imposed stress, leading to progressive growth of the high-shear rate band and consequently to an outward motion of the interface between bands. The development of 3D shear-banding flow due to elastic instability of the high shear rate band is triggered while the proportion of the high-shear rate band keeps growing. This may explain the longer transient since constant rearrangements of Taylor-like vortices are required to adapt their size to the size of the high-shear rate band. In contrast, at imposed shear rate, the interface forms in the bulk, very close to the outer wall over most of the stress plateau, moves inwards up to its final position, which is generally reached faster than under imposed stress and is finally destabilized due to the secondary flows that develop in the high-shear rate band. Interestingly, the way $\dot{\gamma}_h$ reaches its asymptotic value ($\simeq \dot{\gamma}_2$) strongly depends on the control parameter and seems faster when the shear stress is imposed[54]. In this context, probing in a systematic way the banding regime using step stress and shear startup with high space- and time-resolved velocimetry experiments should allow the quantitative test of the elastic instability criterion derived for shear banding systems[39]. Furthermore, the motion of the interface during the transient is supposed to be driven, over a specific time scale, by "diffusive" terms[91]. Indeed, an ad-hoc "diffusive" term with coefficient $\mathcal{D}$ has been introduced to the constitutive models in order to take into account the flow inhomogeneity asso-

Journal of Rheology

ciated with shear banding[25,68]. This coefficient governs the contributions of spatial gradients to the total shear stress and to the dynamics of microstructural order. Experimental estimation of this "diffusion coefficient" has been reported in the literature for shear rate driven shear-banding flows[3,41,77,78] but the stress-controlled counterpart has not been examined. Theoretical predictions of the expected time window and of the corresponding global shear rate evolution where the interface motion is driven by diffusive terms would be a helpful guide for this control parameter.

ACKNOWLEDGMENTS

This work benefited from meetings within the French working group GDR CNRS 2019 'Solliciter La Matière Molle' (SLAMM). The authors thank Thibaut Divoux, Sébastien Manneville and Suzanne Fielding for the critical reading of the manuscript.

[1]Angelico, R., Gentile, L., Ranieri, G. A., and Oliviero Rossi, C., "Flow-induced structures observed in a viscoelastic reverse wormlike micellar system by magnetic resonance imaging and nmr velocimetry," RSC Adv. **6**, 33339–33347 (2016).
[2]Angelico, R., Rossi, C. O., Ambrosone, L., Palazzo, G., Mortensen, K., and Olsson, U., "Ordering fluctuations in a shear-banding wormlike micellar system," Phys. Chem. Chem. Phys. **12**, 8856–8862 (2010).
[3]Ballesta, P., Lettinga, M. P., and Manneville, S., "Superposition rheology of shear-banding wormlike micelles," J. Rheol. **51**, 1047–1072 (2007).
[4]Baravian, C., Benbelkacem, G., and Caton, F., "Using instrumental inertia in controlled stress rheometry," Rheol. Acta **46**, 577–581 (2007).
[5]Baravian, C. and Quemada, D., "Using instrumental inertia in controlled stress rheometry," Rheol. Acta **37**, 223–233 (1998).
[6]Baumert, B. M. and Muller, S. J., "Flow visualization of the elastic taylor-couette instability in boger fluids," Rheologica Acta **34**, 147–159 (1995), 10.1007/BF00398434.
[7]Bécu, L., Anache, D., Manneville, S., and Colin, A., "Evidence for three-dimensional unstable flows in shear-banding wormlike micelles," Phys. Rev. E **76**, 011503 (2007).
[8]Bécu, L., Manneville, S., and Colin, A., "Yielding and flow in adhesive and nonadhesive concentrated emulsions," Phys. Rev. Lett. **96**, 138302 (2006).
[9]Benzi, R., Divoux, T., Barentin, C., Manneville, S., Sbragaglia, M., and Toschi, F., "Unified theoretical and experimental view on transient shear banding," Phys. Rev. Lett. **123**, 248001 (2019).
[10]Benzi, R., Sbragaglia, M., Bernaschi, M., Succi, S., and Toschi, F., "Cooperativity flows and shear-bandings: a statistical field theory approach," Soft Matter **12**, 514–530 (2016).
[11]Berret, J.-F., "Transient rheology of wormlike micelles," Langmuir **13**, 2227–2234 (1997).
[12]Berret, J.-F. and Porte, G., "Metastable versus unstable transients at the onset of a shear-induced phase transition," Phys. Rev. E **60**, 4268–4271 (1999).
[13]Boukany, P. E. and Wang, S.-Q., "A correlation between velocity profile and molecular weight distribution in sheared entangled polymer solutions," J. Rheol. **51**, 217–233 (2007).
[14]Boukany, P. E. and Wang, S.-Q., "Use of particle-tracking velocimetry and flow birefringence to study nonlinear flow behavior of entangled wormlike micellar solution: from wall slip, bulk disentanglement to chain scission," Macromolecules **41**, 1455–1464 (2008), https://doi.org/10.1021/ma702527s.
[15]Boukany, P. E. and Wang, S.-Q., "Shear banding or not in entangled DNA solutions depending on the level of entanglement," J. Rheol. **53**, 73–83 (2009).
[16]Briole, A., Casanellas, L., Fardin, M.-A., Py, C., Cardoso, O., Browaeys, J., and Lerouge, S., "Shear-banding fluids under time-dependent flows: a test of the moorcroft-fielding criteria," Soft Matter , submitted (2021).
[17]Britton, M. M. and Callaghan, P. T., "Two-phase shear band structures at uniform stress," Phys. Rev. Lett. **78**, 4930–4933 (1997).
[18]Callaghan, P. T., "Rheo nmr and shear banding," Rheol. Acta **47**, 243–255 (2008).
[19]Cappelaere, E. and Cressely, R., "Rheological behavior of an elongated micellar solution at low and high salt concentrations," Colloid and Polymer Science **276**, 1059–1056 (1998).
[20]Casanellas, L., Dimitriou, C., Ober, T., and McKinley, G., "Spatiotemporal dynamics of multiple shear-banding events for viscoelastic micellar fluids in cone-plate shearing flows," J. non-Newt. Fluid Mech. , 234–247 (2015).
[21]Coussot, P., Nguyen, Q. D., Huynh, H. T., and Bonn, D., "Avalanche behavior in yield stress fluids," Phys. Rev. Lett. **88**, 175501 (2002).
[22]Cromer, M., Fredrickson, G. H., and Leal, L. G., "A study of shear banding in polymer solutions," Physics of Fluids **26**, 063101 (2014), https://doi.org/10.1063/1.4878842.
[23]Cromer, M., Villet, M. C., Fredrickson, G. H., and Leal, L. G., "Shear banding in polymer solutions," Physics of Fluids **25**, 051703 (2013), https://doi.org/10.1063/1.4805089.
[24]Decruppe, J. P., Lerouge, S., and Berret, J. F., "Insight in shear banding under transient flow," Phys. Rev. E **63**, 022501 (2001).
[25]Dhont, J. K. G., "A constitutive relation describing the shear-banding transition," Phys. Rev. E **60**, 4534–4544 (1999).
[26]Divoux, T., Barentin, C., and Manneville, S., "From transient fluidization processes to herschel-bulkley behavior in simple yield stress fluids," Soft Matter **7**, 8409–8418 (2011).
[27]Divoux, T., Barentin, C., and Manneville, S., "Stress overshoot in a simple yield stress fluid: an extensive study combining rheology and velocimetry," Soft Matter **7**, 9335–9349 (2011).
[28]Divoux, T., Fardin, M. A., Manneville, S., and Lerouge, S., "Shear banding of complex fluids," Annual Review of Fluid Mechanics **48**, 81–103 (2016), https://doi.org/10.1146/annurev-fluid-122414-034416.
[29]Divoux, T., Tamarii, D., Barentin, C., and Manneville, S., "Transient shear banding in a simple yield stress fluid," Phys. Rev. Lett. **104**, 208301 (2010).
[30]Eberle, A. P. and Porcar, L., "Flow-sans and rheo-sans applied to soft matter," Current Opinion in Colloid & Interface Science **17**, 33–43 (2012).
[31]Ewoldt, R. H., Johnston, M. T., and Caretta, L. M., "Experimental challenges of shear rheology: How to avoid bad data," in *Complex Fluids in Biological Systems: Experiment, Theory, and Computation*, edited by S. E. Spagnolie (Springer New York, New York, NY, 2015) pp. 207–241.
[32]Ewoldt, R. H., Winegard, T. M., and Fudge, D. S., "Non-linear viscoelasticity of hagfish slime," International Journal of Non-Linear Mechanics **46**, 627 – 636 (2011), special issue on non-linear mechanics of biological structures.
[33]Fardin, M., Divoux, T., Guedeau-Boudeville, M., Buchet-Maulien, I., Browaeys, J., McKinley, G., Manneville, S., and Lerouge, S., "Shear-banding in surfactant wormlike micelles: elastic instabilities and wall slip," Soft Matter **8**, 2535–2553 (2012).
[34]Fardin, M., Ober, T., Gay, C., Grégoire, G., McKinley, G., and Lerouge, S., "Potential ways of thinking about the shear-banding phenomenon," Soft Matter **8**, 910–922 (2012).
[35]Fardin, M.-A., Casanellas, L., Saint-Michel, B., Manneville, S., and Lerouge, S., "Shear-banding in wormlike micelles: Beware of elastic instabilities," J. Rheol. **60**, 917–926 (2016), https://doi.org/10.1122/1.4960333.
[36]Fardin, M. A., Lasne, B., Cardoso, O., Grégoire, G., Argentina, M., Decruppe, J. P., and Lerouge, S., "Taylor-like vortices in shear-banding flow of giant micelles," Phys. Rev. Lett. **103**, 028302 (2009).
[37]Fardin, M.-A. and Lerouge, S., "Instabilities in wormlike micelle systems," The Eur. Phys. J. E **35**, 1–29 (2012).

[38]Fardin, M.-A. and Lerouge, S., "Flows of living polymer fluids," Soft Matter **10**, 8789–8799 (2014).
[39]Fardin, M. A., Ober, T. J., Gay, C., Grégoire, G., McKinley, G. H., and Lerouge, S., "Criterion for purely elastic taylor-couette instability in the flows of shear-banding fluids," Eur. Phys. Lett. **96**, 44004 (2011).
[40]Fardin, M. A., Ober, T. J., Grenard, V., Divoux, T., Manneville, S., McKinley, G. H., and Lerouge, S., "Interplay between elastic instabilities and shear-banding: three categories of Taylor-Couette flows and beyond," Soft Matter **8**, 10072–10089 (2012).
[41]Fardin, M.-A., Radulescu, O., Morozov, A., Cardoso, O., Browaeys, J., and Lerouge, S., "Stress diffusion in shear banding wormlike micelles," J. Rheol. **59**, 1335–1362 (2015), https://doi.org/10.1122/1.4930858.
[42]Feindel, K. W. and Callaghan, P. T., "Anomalous shear banding: multidimensional dynamics under fluctuating slip conditions," Rheol. Acta **49**, 1003–1013 (2010).
[43]Fielding, S. M., "Complex dynamics of shear banded flows," Soft Matter **3**, 1262–1279 (2007).
[44]Fielding, S. M., "Viscoelastic taylor-couette instability of shear banded flow," Phys. Rev. Lett. **104**, 198303 (2010).
[45]Fielding, S. M., "Triggers and signatures of shear banding in steady and time-dependent flows," J. Rheol. **60**, 821–834 (2016), https://doi.org/10.1122/1.4961480.
[46]Fielding, S. M. and Olmsted, P. D., "Early stage kinetics in a unified model of shear-induced demixing and mechanical shear banding instabilities," Phys. Rev. Lett. **90**, 224501 (2003).
[47]Gibaud, T., Barentin, C., and Manneville, S., "Influence of boundary conditions on yielding in a soft glassy material," Phys. Rev. Lett. **101**, 258302 (2008).
[48]Gibaud, T., Frelat, D., and Manneville, S., "Heterogeneous yielding dynamics in a colloidal gel," Soft Matter **6**, 3482–3488 (2010).
[49]Grand, C., Arrault, J., and Cates, M. E., "Slow transients and metastability in wormlike micelles," J. Phys. II France **7**, 1071–1086 (1997).
[50]Grenard, V., Divoux, T., Taberlet, N., and Manneville, S., "Timescales in creep and yielding of attractive gels," Soft Matter **10**, 1555–1571 (2014).
[51]Gurnon, A. K., Lopez-Barron, C., Wasbrough, M. J., Porcar, L., and Wagner, N. J., "Spatially resolved concentration and segmental flow alignment in a shear-banding solution of polymer-like micelles," ACS Macro Letters **3**, 276–280 (2014), http://pubs.acs.org/doi/pdf/10.1021/mz5000152.
[52]Gurnon, A. K., Lopez-Barron, C. R., Eberle, A. P. R., Porcar, L., and Wagner, N. J., "Spatiotemporal stress and structure evolution in dynamically sheared polymer-like micellar solutions," Soft Matter **10**, 2889–2898 (2014).
[53]Helfand, E. and Fredrickson, G. H., "Large fluctuations in polymer solutions under shear," Phys. Rev. Lett. **62**, 2468–2471 (1989).
[54]Hu, Y. T. and Lips, A., "Kinetics and mechanism of shear banding in an entangled micellar solution," J. Rheol. **49**, 1001–1027 (2005).
[55]Hu, Y. T., Palla, C., and Lips, A., "Comparison between shear banding and shear thinning in entangled micellar solutions," J. Rheol. **52**, 379–400 (2008).
[56]Jaradat, S., Harvey, M., and Waigh, T. A., "Shear-banding in polyacrylamide solutions revealed via optical coherence tomography velocimetry," Soft Matter **8**, 11677–11686 (2012).
[57]Kadoma, I. A. and van Egmond, J. W., "Shear-enhanced orientation and concentration fluctuations in wormlike micelles: Effect of salt," Langmuir **13**, 4551–4561 (1997).
[58]Kunita, I., Sato, K., Tanaka, Y., Takikawa, Y., Orihara, H., and Nakagaki, T., "Shear banding in an f-actin solution," Phys. Rev. Lett. **109**, 248303 (2012).
[59]Kurokawa, A., Vidal, V., Kurita, K., Divoux, T., and Manneville, S., "Avalanche-like fluidization of a non-brownian particle gel," Soft Matter **11**, 9026–9037 (2015).
[60]Larson, R. G., Shaqfeh, E. S. G., and Muller, S. J., "A purely elastic transition in taylor-couette flow," J. Fluid Mech. **218**, 573–600 (1990).
[61]Lee, J. Y., Fuller, G. G., Hudson, N. E., and Yuan, X.-F., "Investigation of shear-banding structure in wormlike micellar solution by pointwise flow-induced birefringence measurements," J. Rheol. **49**, 537–550 (2005).
[62]Lerouge, S. and Berret, J.-F., "Shear-induced transitions and instabilities in surfactant wormlike micelles," Adv Polym Sci **230**, 1–71 (2010).
[63]Lerouge, S., Decruppe, J.-P., and Berret, J.-F., "Correlation between rheological and optical properties of micellar solution under shear banding flow," Langmuir **16**, 6464–6474 (2000).
[64]Lerouge, S., Decruppe, J.-P., and Humbert, C., "Shear banding in a micellar solution under transient flow," Phys. Rev. Lett. **81**, 5457–5460 (1998).
[65]Lerouge, S., Decruppe, J.-P., and Olmsted, P., "Birefringence banding in a micellar solution or the complexity of heterogeneous flows," Langmuir **20**, 11355–11365 (2004).
[66]Lerouge, S., Fardin, M. A., Argentina, M., Gregoire, G., and Cardoso, O., "Interface dynamics in shear-banding flow of giant micelles," Soft Matter **4**, 1808–1819 (2008).
[67]Lerouge, S. and Olmsted, P. D., "Non-local effects in shear banding of polymeric flows," Frontiers in Physics **7**, 246 (2020).
[68]Lerouge, S. and Olmsted, P. D., "Non-local effects in shear banding of polymeric flows," Frontiers in Physics **7**, 246 (2020).
[69]Lettinga, M. P. and Manneville, S., "Competition between shear banding and wall slip in wormlike micelles," Phys. Rev. Lett. **103**, 248302 (2009).
[70]López-Barrón, C. R., Gurnon, A. K., Eberle, A. P. R., Porcar, L., and Wagner, N. J., "Microstructural evolution of a model, shear-banding micellar solution during shear startup and cessation," Phys. Rev. E **89**, 042301 (2014).
[71]López-González, M. R., Holmes, W. M., Callaghan, P. T., and Photinos, P., "Shear banding fluctuations and nematic order in wormlike micelles," Phys. Rev. Lett. **93**, 268302 (2004).
[72]López-González, M. R., Holmes, W. M., Callaghan, P. T., and Photinos, P. J., "Rheo-nmr phenomena of wormlike micelles," Soft Matter **2**, 855–869 (2006).
[73]Mair, R. W. and Callaghan, P. T., "Shear flow of wormlike micelles in pipe and cylindrical couette geometries as studied by nuclear magnetic resonance microscopy," J. Rheol. **41**, 901–923 (1997).
[74]Manneville, S., "Recent experimental probes of shear banding," Rheol. Acta **47**, 301–318 (2008).
[75]Manneville, S., Colin, A., Waton, G., and Schosseler, F., "Wall slip, shear banding, and instability in the flow of a triblock copolymer micellar solution," Phys. Rev. E **75**, 061502 (2007).
[76]Martin, J. and Hu, Y., "Transient and steady-state shear banding in aging soft glassy materials," Soft Matter **8**, 6940–6949 (2012).
[77]Masselon, C., Colin, A., and Olmsted, P. D., "Influence of boundary conditions and confinement on nonlocal effects in flows of wormlike micellar systems," Phys. Rev. E **81**, 021502 (2010).
[78]Masselon, C., Salmon, J.-B., and Colin, A., "Nonlocal effects in flows of wormlike micellar solutions," Phys. Rev. Lett. **100**, 038301 (2008).
[79]Miller, E. and Rothstein, J. P., "Transient evolution of shear-banding wormlike micellar solutions," J. Non-Newt. Fluid Mech. **143**, 22–37 (2007).
[80]Milner, S., McLeish, T., and Likhtman, A., "Microscopic theory of convective constraint release," J. Rheol. **45**, 539–563 (2001).
[81]Moorcroft, R. and Fielding, S., "Criteria for shear banding in time-dependent flows of complex fluids," Phys. Rev. Lett. **110**, 086001 (2013).
[82]Moorcroft, R. L. and Fielding, S. M., "Shear banding in time-dependent flows of polymers and wormlike micelles," J. Rheol. **58**, 103–147 (2014), https://doi.org/10.1122/1.4842155.
[83]Morozov, A. N. and van Saarloos, W., "An introductory essay on subcritical instabilities and the transition to turbulence in viscoelastic parallel shear flows," Phys. Rep. **447**, 112–143 (2007).
[84]Muller, S. J., "Elastically-influenced instabilities in taylor-couette and other flows with curved streamlines: a review," Korea-Aust. Rheol. Journal **20**, 117–125 (2008).
[85]Nicolas, A. and Morozov, A., "Nonaxisymmetric instability of shear-banded taylor-couette flow," Phys. Rev. Lett. **108**, 088302 (2012).
[86]Pakdel, P. and McKinley, G. H., "Elastic instability and curved streamlines," Phys. Rev. Lett. **77**, 2459–2462 (1996).

[87]Paredes, J., Shahidzadeh-Bonn, N., and Bonn, D., "Shear banding in thixotropic and normal emulsions," J. Phys.: Condens. Matter **23**, 284116 (2011).
[88]Perge, C., Fardin, M.-A., and Manneville, S., "Inertio-elastic instability of non shear-banding wormlike micelles," Soft Matter **10**, 1450–1454 (2014).
[89]Perge, C., Fardin, M.-A., and Manneville, S., "Surfactant micelles: model systems for flow instabilities of complex fluids," Eur. Phys. J. E **37**, 23–34 (2014).
[90]Pipe, C. J., Kim, N. J., Vasquez, P. A., Cook, L. P., and McKinley, G. H., "Wormlike micellar solutions: Ii. comparison between experimental data and scission model predictions," Journal of Rheology **54**, 881–913 (2010), https://doi.org/10.1122/1.3439729.
[91]Radulescu, O., Olmsted, P. D., Decruppe, J.-P., Lerouge, S., Berret, J.-F., and Porte, G., "Time scales in shear banding of wormlike micelles," Europhys. Lett. **62**, 230–236 (2003).
[92]Rehage, H. and Hoffmann, H., "Viscoelastic surfactant solutions: model systems for rheological research," Mol. Phys. **74**, 933–973 (1991).
[93]Rogers, S., Callaghan, P., Petekidis, G., and Vlassopoulos, D., "Time-dependent rheology of colloidal star glasses," J. Rheol. **54**, 133–158 (2010).
[94]Rogers, S. A., Vlassopoulos, D., and Callaghan, P. T., "Aging, yielding, and shear banding in soft colloidal glasses," Phys. Rev. Lett. **100**, 128304 (2008).
[95]Salmon, J.-B., Colin, A., Manneville, S., and Molino, F., "Velocity profiles in shear-banding wormlike micelles," Phys. Rev. Lett. **90**, 228303 (2003).
[96]Salmon, J.-B., Manneville, S., and Colin, A., "Shear banding in a lyotropic lamellar phase. i. time-averaged velocity profiles," Phys. Rev. E **68**, 051503 (2003).
[97]Salmon, J.-B., Manneville, S., and Colin, A., "Shear banding in a lyotropic lamellar phase. ii. temporal fluctuations," Phys. Rev. E **68**, 051504 (2003).
[98]Spenley, A., Cates, M. E., and McLeish, T. C. B., "Nonlinear rheology of wormlike micelles," Phys. Rev. Lett. **71**, 939–942 (1993).
[99]Spenley, A., Yuan, X. F., and Cates, M. E., "Nonmonotonic constitutive laws and the formation of shear-banded flows," J. Phys. II France **6**, 551–571 (1996).
[100]Thareja, P., Hoffmann, I. H., Liberatore, M. W., Helgeson, M. E., Hu, Y. T., Gradzielski, M., and Wagner, N. J., "Shear-induced phase separation (sips) with shear banding in solutions of cationic surfactant and salt," Journal of Rheology **55**, 1375–1397 (2011), https://doi.org/10.1122/1.3641517.
[101]White, J. and Muller, S., "Viscous heating and the stability of newtonian and viscoelastic taylor-couette flows," Physical Review Letters **84**, 5130 (2000).
[102]White, J. and Muller, S., "Experimental studies on the effect of viscous heating on the hydrodynamic stability of viscoelastic taylor-couette flow," J. Rheol. **47**, 1467 (2003).
[103]Yao, N. Y., Larsen, R. J., and Weitz, D. A., "Probing nonlinear rheology with inertio-elastic oscillations," J. Rheol. **52**, 1013–1025 (2008), times Cited: 17.
[104]Yerushalmi, J., Katz, S., and Shinnar, R., "Stability of steady shear flows of some viscoelastic fluids," Chemical Engineering Science **25**, 1891 (1970).

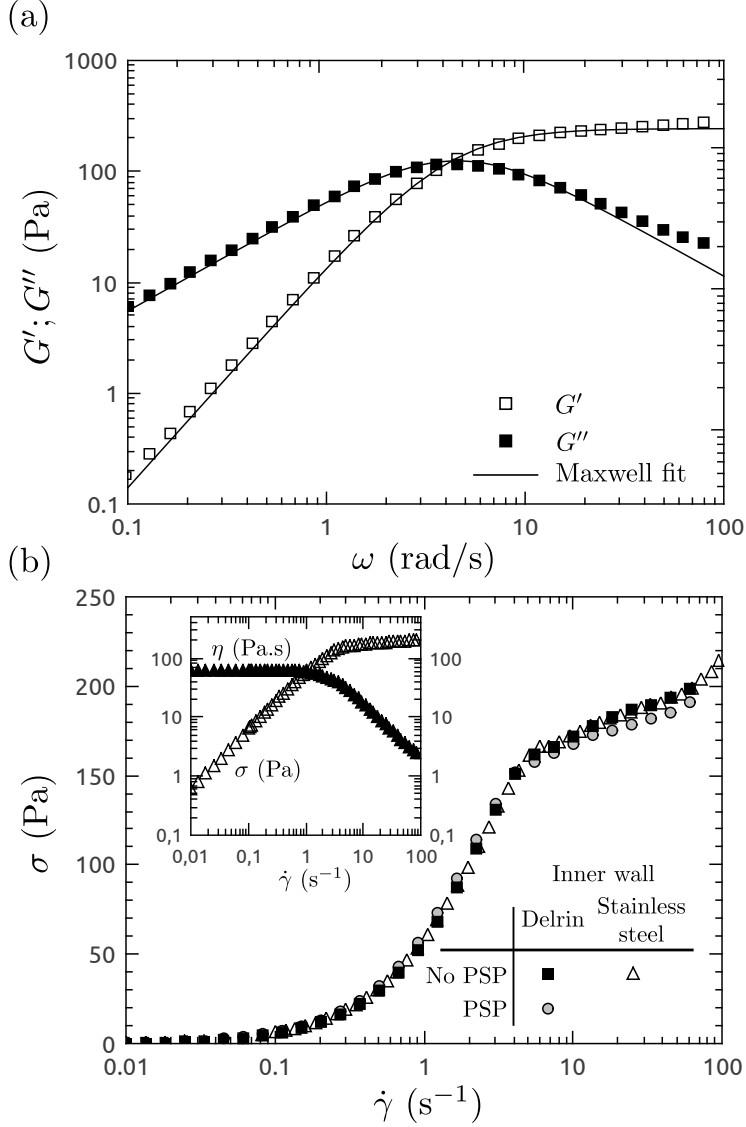

πάντα ῥεῖ

Journal of Rheology

ACCEPTED MANUSCRIPT

PLEASE CITE THIS ARTICLE AS DOI: 10.1122/8.0000303

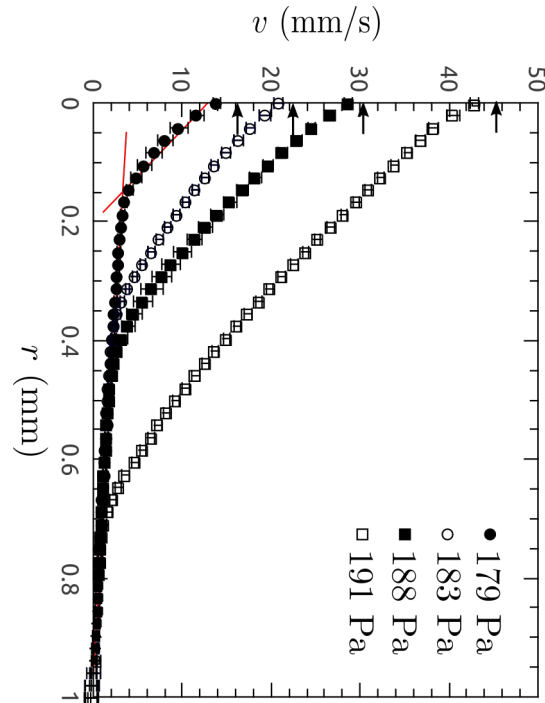

Journal of Rheology

(a)

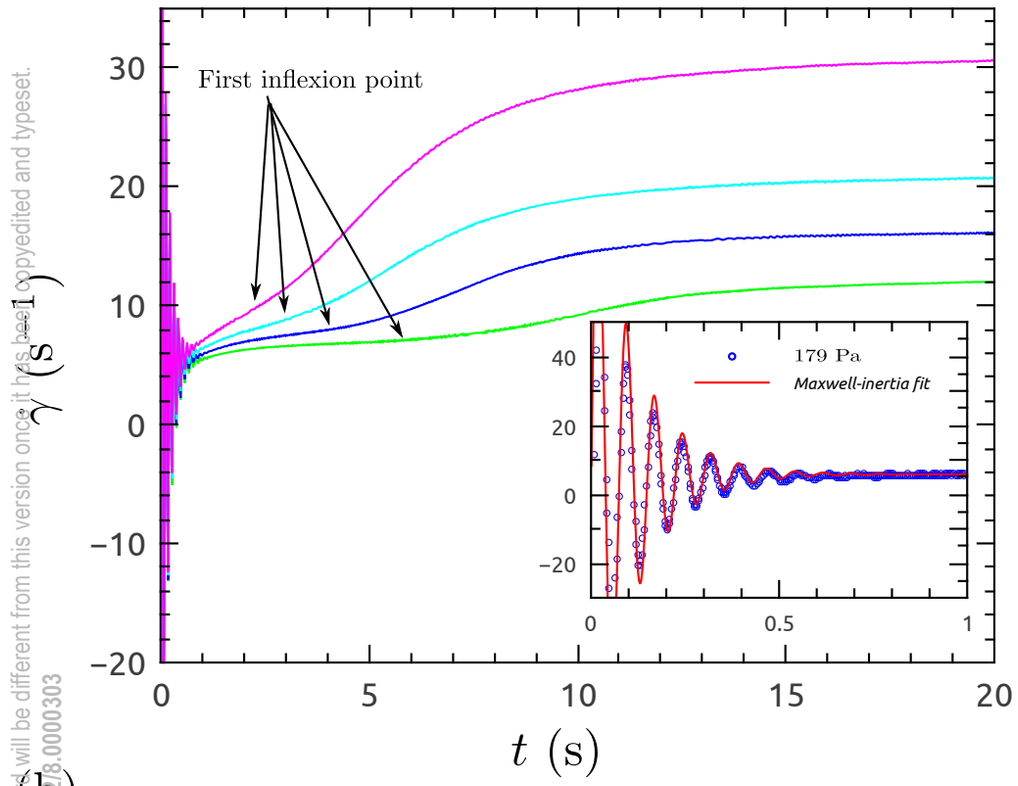

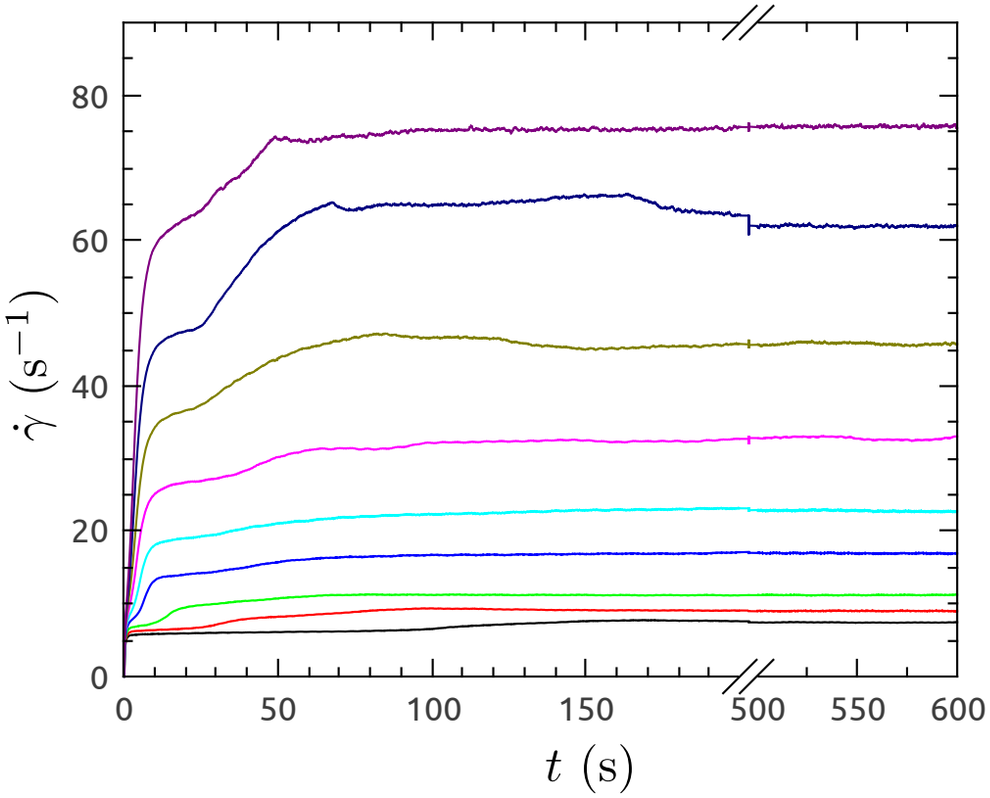

(b)

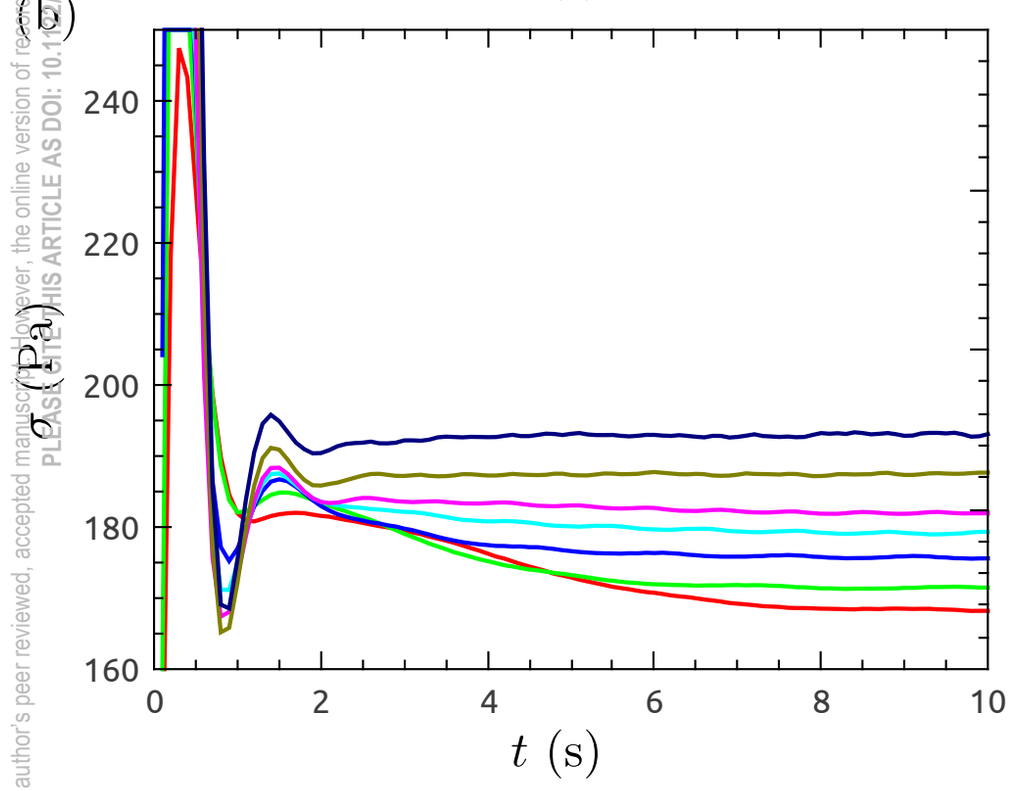

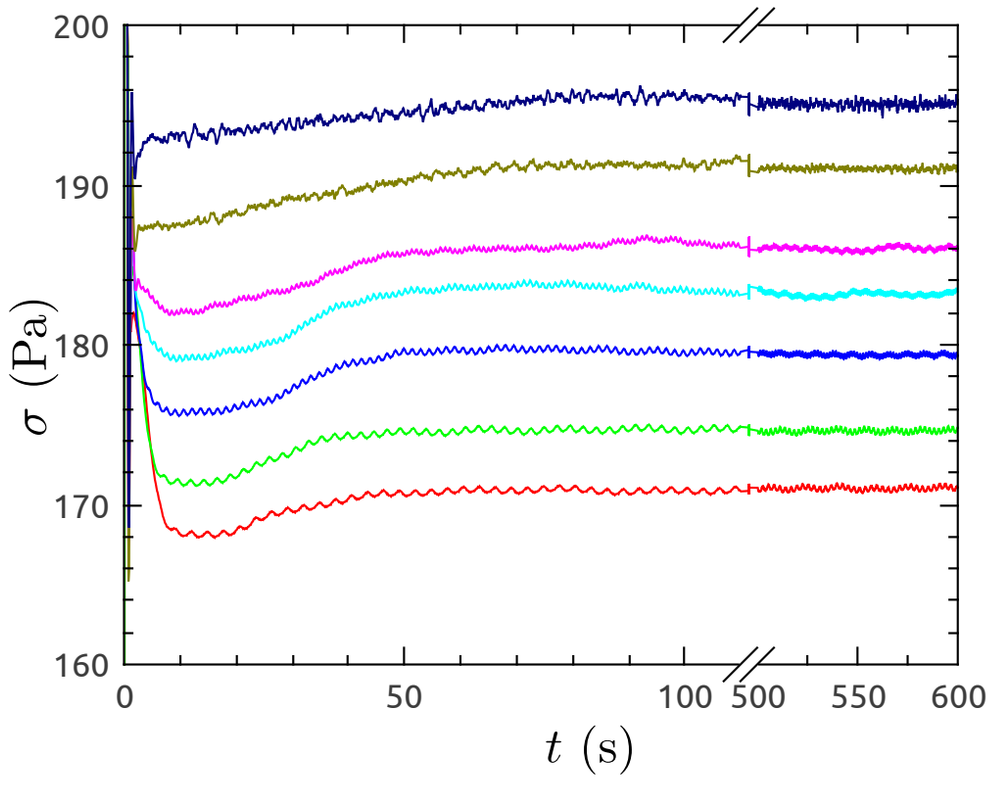

Journal of Rheology

(a) $\sigma = 183$ Pa

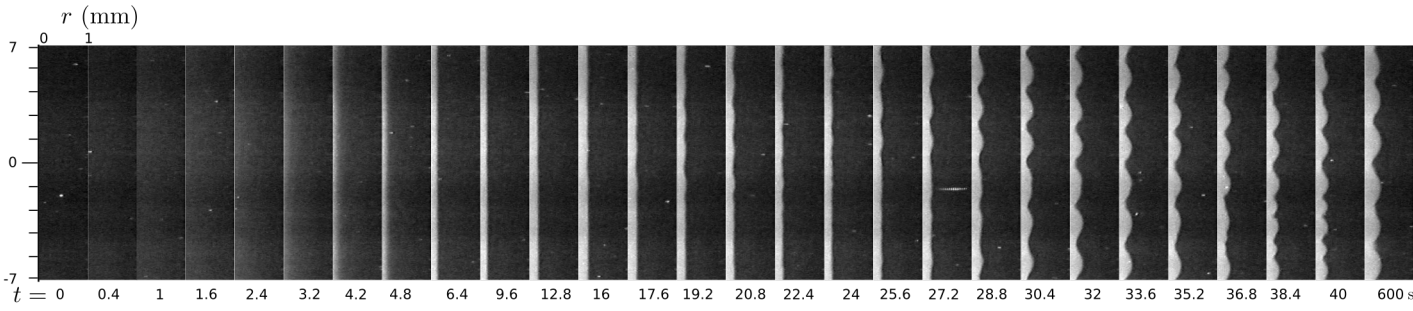

(b) $\dot{\gamma} = 23$ s^{-1}

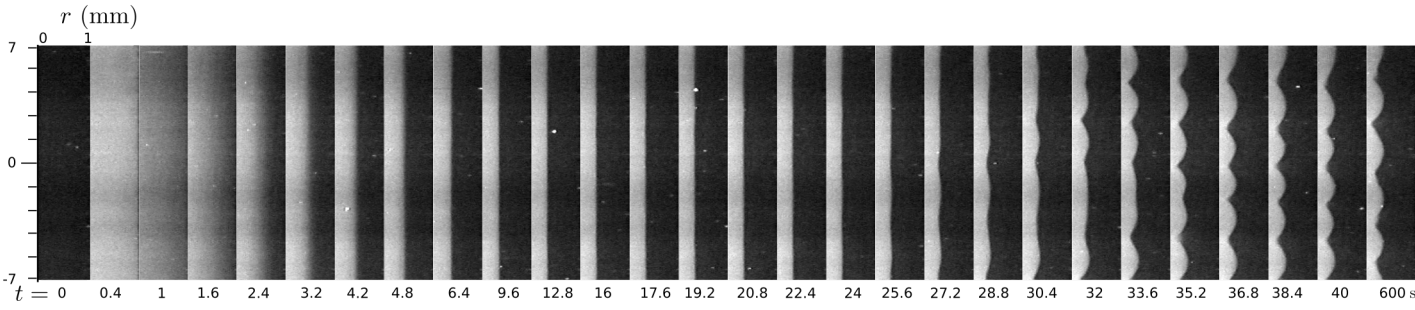

Journal of Rheology

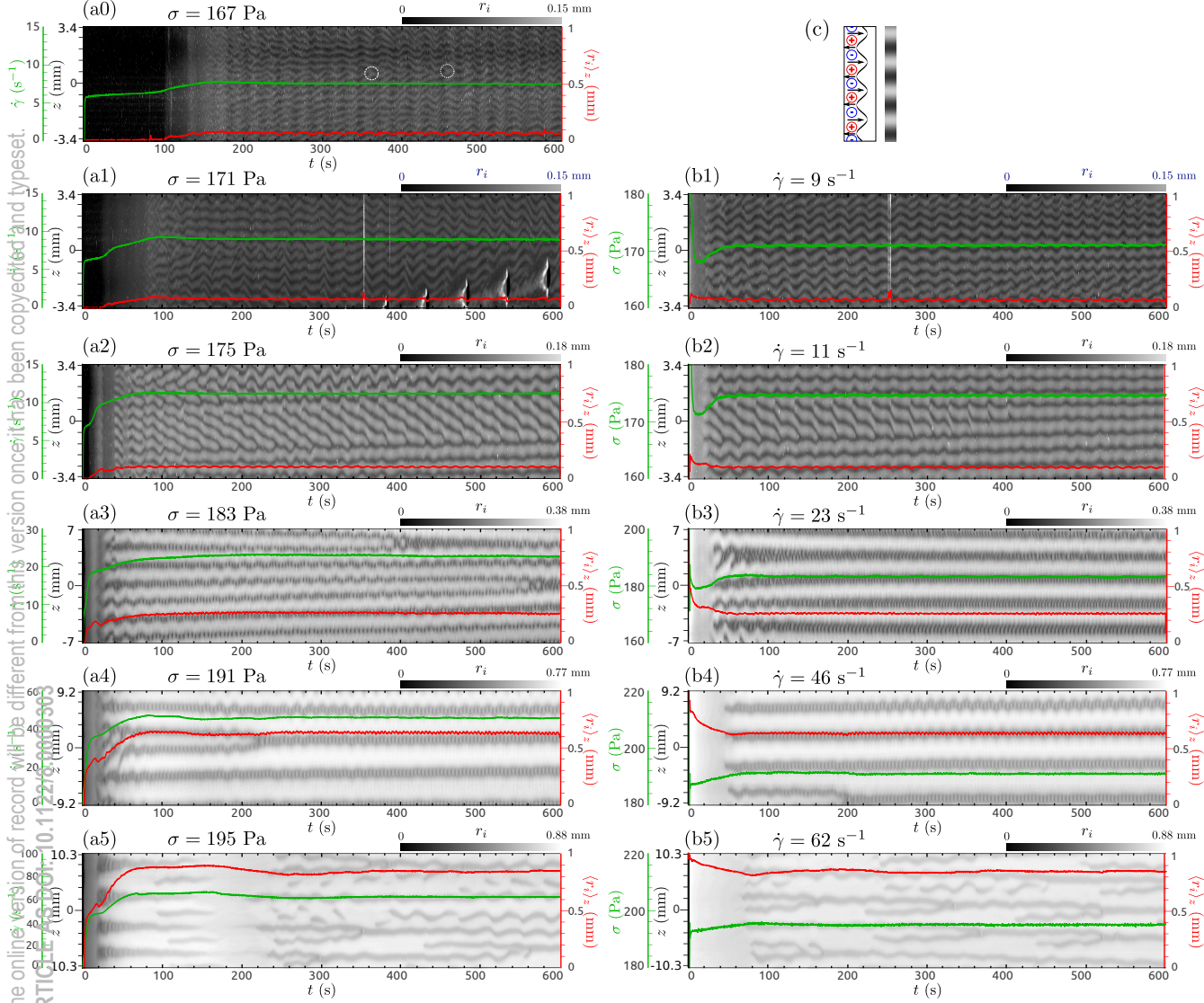

(a)

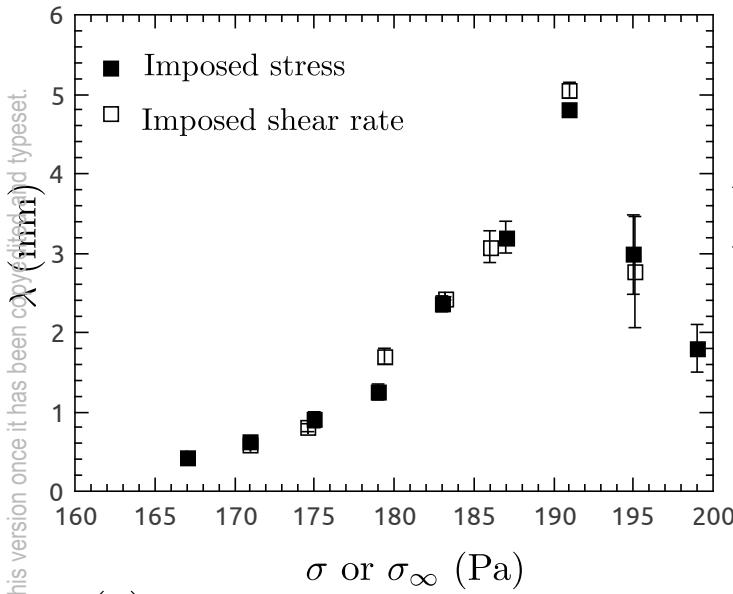

(b)

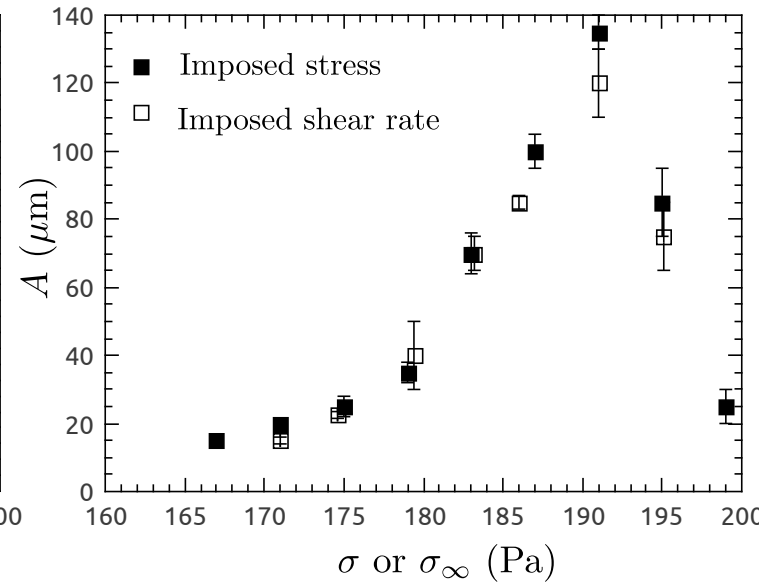

(c)

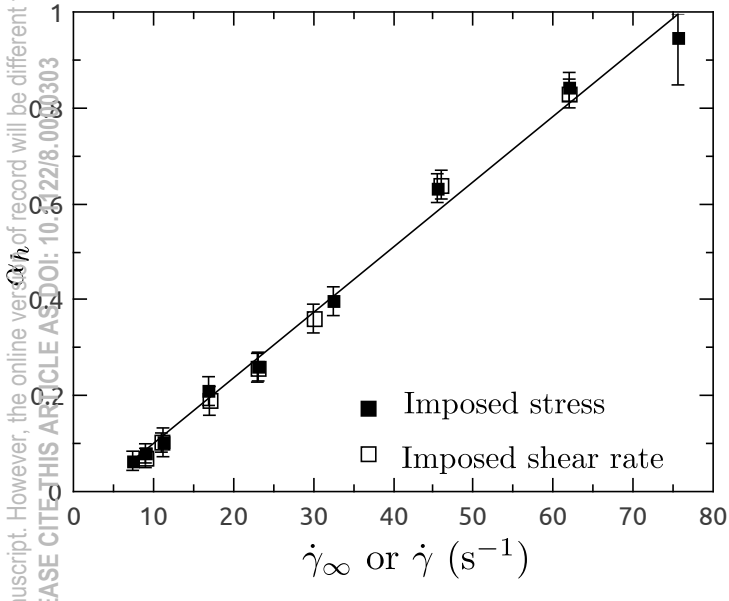

(d)